Generalized Three Dimensional Geometrical Scattering Channel Model for Indoor and Outdoor Propagation Environments

by

Mohammad A. S. Alsehaili

A Thesis submitted to the Faculty of Graduate Studies of
The University of Manitoba
in partial fulfilment of the requirements of the degree of

DOCTOR OF PHILOSOPHY

Department of Electrical and Computer Engineering
The University of Manitoba
Winnipeg, Manitoba, Canada

To my ***parents***

To my wife, ***Aljoharh***

To my children: ***Abdullah****,* ***Alanoud*** *and* ***Algaliah***

To all members of my family, particularly,

my uncles: ***Mohammad*** *and* ***Ali****, and my brother* ***Ali***

Acknowledgment

I am deeply indebted to my supervisors, Dr. Sima Noghanian, Dr. Abdel Razik Sebak and Dr. Douglas Buchanan, who provided me with a great deal of assistance, encouragement and support. This thesis would not have been possible without them.

I am also indebted to the members of the advisory committee, Dr. Attahiru Sule Alfa and Dr. Tarek ElMekkawy, for all their valuable suggestions and help.

Without the support of some of very close friends over the past few years this work would not have been completed. I would like to thank, particularly my parents, my wife, Aljoharh and my brothers: Ali and Abdullah for all their encouragement and continues support, both emotionally and financially.

Finally, I must acknowledge the Saudi Arabia Government for providing me the scholarship to complete my Doctor degree.

Abstract

The well known geometrical scattering channel modeling technique has been suggested to describe the spatial statistical distribution of the received multipath signals at various types of wireless communication environments and for different wireless system applications. This technique is based on the assumption that the scatterers, i.e. objects that give rise to the multipath signals, are randomly distributed within a specified geometry that may include the base station and/or the mobile station. The geometrical scattering channel models can provide convenient and simple statistical functions for some of the important physical quantities of the received multipath fading signals, such as: angle of arrival, time of arrival, angular spread, delay spread and the spatial correlation function.

In this thesis, a new three dimensional geometrical scattering channel model has been developed for outdoor and indoor wireless communication environments. The probability density functions of the angle of arrival of the received multipath signals are provided in compact forms. These functions facilitate independent control of the angular spread in both the azimuth and the elevation angles via the model's parameters. To establish the model verification, the developed model has been compared against the results from a site-specific propagation prediction technique in indoor and outdoor wireless communication environments.

The developed three dimensional model has been extended to include the temporal statistical distribution of the received multipath signals for uniform and non-uniform distributions of the scatterer. Several of the probability density functions of the angle of arrival and time

of arrival of the received multipath signals are provided. The probability density functions of the angle of arrival have been validated by comparing them against the results from real channel measurements data. In addition, the developed three dimensional geometrical scattering channel model has been extended for multiple input multiple output wireless channel modeling applications. A three dimensional spatial correlation function has been developed in terms of some of the physical channel's parameters, such as: displacements and orientation of the employed antenna elements. The developed correlation function has been used to simulate and investigate the performance of wireless multiple input multiple output systems in different scenarios.

List of Symbols

a	Ellipsoid's semi-length on the x-axis
b	Ellipsoid's semi-length on the y-axis
B	Channel bandwidth
c	Ellipsoid's semi-length on the z-axis
D	Distance between the base station and the mobile station antennas
e	Spheroid and ellipse eccentricity
e_1	Ellipsoid's eccentricity in the azimuth angle
e_2	Ellipsoid's eccentricity in the elevation angle
g	Amplitude of the multipath signals
f	Ellipsoid, spheroid and ellipse's focal length
H	Channel transfer matrix
H_{BS}	Height of the base station antenna
H_{MS}	Height of the mobile station antenna
$i.i.d$	Independently Identically Distributed
h_{kq}	The gain between the base station antenna k and the mobile station antenna q
I_{N_r}	$N_r \times N_r$ Identity matrix
N	Minimum number of transmitting and receiving antenna elements
N_t	Number of transmitting antenna elements
N_r	Number of receiving antenna elements
R	Radius of the circle
R_r	Receiving correlation matrix
R_t	Transmitting correlation matrix

r_k	Distance between the receiving antenna element k to the scatterer
r_l	Distance between the receiving antenna element l to the scatterer
r_q	Distance between the transmitting antenna element q to the scatterer
r_p	Distance between the transmitting antenna element p to the scatterer
S	Number of scatterers
r_m	Distance between the scatterer and the center of the antenna array at the mobile station
r_b	Distance between the scatterer and the center of the antenna array at the base station
V	Ellipsoid's volume
V_τ	Spheroid's volume corresponding to time of arrival τ
$V_{\tau_{max}}$	Spheroid's volume corresponding to time of arrival τ_{max}

α	Spheroid's inclination angle
α_{kl}	Orientation angle of the elements k and l in the elevation angle at the mobile station
α_{pq}	Orientation angle of the elements p and q in the elevation angle at the base station
β_{kl}	Orientation angle of the elements k and l in the azimuth angle at the mobile station
β_{pq}	Orientation angle of the elements p and q in the azimuth angle at the base station
δ_{kl}	Distance between elements k and l at the mobile station
δ_{pq}	Distance between elements p and q at the base station
θ_b	Angle of arrival in the elevation angle at the base station
θ_m	Angle of arrival in the elevation angle at the mobile station
σ_τ	Delay spread
σ_Ω	Angular spread
σ_ϕ	Angular spread in the azimuth angle
σ_θ	Angular spread in the elevation angle

ρ	Correlation coefficient
τ	Time of arrival
τ_0	Time of arrival of the line of sight signal
τ_{max}	Maximum observation time
τ_δ	Small value of the time of arrival
ϕ_b	Angle of arrival in the azimuth angle at the base station
ϕ_m	Angle of arrival in the azimuth angle at the mobile station
Ψ	Phase of the multipath signal
Ω_{kq}	Total power of the link between antenna elements k and q

List of Abbreviations

1G	First Generation
2G	Second Generation
3G	Third Generation
4G	Fourth Generation
2D	Two Dimensional
3D	Three Dimensional
3dB	Three Decibel
AOA	Angle of Arrival
BS	Base Station
CDMA	Code Division Multiple Access
CDF	Cumulative Distribution Function
DOD	Direction Of Departure
FDMA	Frequency Division Multiple Access
ISI	InterSymbol Interference
LOS	Line Of Sight
MEA	Multiple Element Antenna
MISO	Multiple Input Single Output
MIMO	Multiple Input Multiple Output
MS	Mobile Station
pdf	Probability Density Function
pmf	Probability Mass Function
Rx	Receiver
RMS	Root Mean Square

SISO	Single Input Single Output
SIMO	Single Input Multiple Output
SDMA	Space Division Multiple Access
SNR	Signal to Noise Ratio
TOA	Time of Arrival
TDMA	Time Division Multiple Access
Tx	Transmitter
WLAN	Wireless Local Area Network
Wi-Fi	Wireless Fidelity
WiMAX	Worldwide Interoperability for Microwave Access

Table of Contents

List of Figures

Chapter 1

Introduction

1.1 Preface

Over the last two decades, wireless communication systems have been developed to provide sophisticated communication services for anyone, anytime, and anywhere throughout the world. The mid 1980s saw the beginning of the first generation systems (1G), which was based on analog technology and was limited to voice communication services. Digital technology was later introduced into wireless communication systems at the beginning of the 1990s, starting with the second generation systems (2G) and evolving toward the currently deployed third generation (3G) and fourth generation (4G) systems. These advanced systems, i.e. 3G and beyond, promise to provide a multitude of communication services such as voice, data, and streaming multimedia [1, 2]. However, the increasing demand for higher data rates and communication link reliability, coupled by the limited radio frequency spectrum, has led to the need for the development of new techniques that help to overcome these limitations, as well as, satisfy the increasing demands in future systems. Exploiting the spatial dimension at one or both ends of wireless communications link is considered as one of the most vital technologies that promises to aid in the realization of future demands of wireless services without the need of additional spectrum resources [1–5].

1.2 Motivation

Typically, radio propagation conditions have an observed influence on the performance of wireless communication systems, especially systems that utilize the spatial dimension. In multipath wireless channels, the transmission paths from the transmitter to the receiver may vary from a simple line of sight (LOS) path to one that is severely obstructed by objects in the propagation environment. These objects give rise to different propagation mechanisms, such as: scattering, reflections, diffractions and transmissions of the propagated signal within the wireless channel medium. In multipath communication environments, the received signal is comprised of a number of constructively and destructively interfering copies of the transmitted signal. Since the multipath signals propagate along different paths to reach their destination and the properties of the transmission environment vary from path to path, each component experiences differences in properties, such as: power, phase shift, angle of arrival (AOA), time of arrival (TOA) and polarization. Therefore, multipath propagation signals are considered to be an undesirable feature of radio channels, as the performance, i.e. reliability, of a conventional single input single output (SISO) wireless communication system may be limited by these multipath signals by introducing fading and interferences [1, 3]. In such cases, multiple element antenna (MEA) systems have been employed at the receiver in single input multiple output (SIMO) wireless systems, i.e. receive diversity, or at the transmitter in multiple input single output (MISO) wireless systems, i.e. transmit diversity, to mitigate the undesirable effects of multipath signals [1,5–8]. On the other hand, multipath propagation signals in a rich scattering environment may be considered to be advantageous because they can be exploited to increase the performance of the wireless communication systems by employing the MEA system at both the receiver and the transmitter, i.e. spatial multiplexing, along with appropriate space-time signal processing [9–15]. The use of the MEA system at both the receiver and the transmitter is known as a multiple input multiple output (MIMO) wireless system. Therefore, the MEA system can be used at one or both ends of wireless communication link to realize the utilization of the spatial dimension.

In wireless communication systems which utilize the spatial dimension, the angular statistical distributions of the received multipath signals are beneficial in determining the performance of the radio link. These distributions can be obtained from real channel measured data and/or from site specific propagation prediction data. However, normally these data are unavailable and/or unapplicable [3]. Therefore, having a simple channel model that is capable of providing both spatial and temporal characteristics of the received multipath signals is useful in order to evaluate, analyze, and design advanced wireless communication systems. The well known geometrical scattering channel modeling technique has been developed to describe the statistical distributions of the received multipath signals in various types of wireless communication environments and for different wireless system applications.

The geometrical scattering channel models are based on the assumption that the scatterers, i.e. objects that cause multipath signals, are randomly distributed within two dimensional (2D) or three dimensional (3D) space, i.e. 2D or 3D models, that are limited by a specified geometry that may include the base station (BS) and/or the mobile station

(MS). The geometrical models can lead to convenient, simple statistical distributions for some important physical quantities, such as AOA, TOA, angular spread, delay spread and the space-time correlation function of the received multipath fading signals. Fast and easy implementation of the wireless channel impulse response based on the statistical distributions of the received multipath signals can be obtained for both SISO and MIMO wireless communication systems. The 3D statistical distribution information of the received multipath signals can provide accurate modeling for wireless channel impulse response. This enables wireless system designers to create wireless communication systems more efficiently in terms of some wireless channel parameters, such as: receiver signal to noise ratio (SNR), bit-error-rate (BER) performance, capacity, channel access, co-channel interference cancelation, equalization, diversity, modulation performance tradeoffs, and cost. This 3D model can be used to describe the angular and temporal statistical distribution of the multipath signals in outdoor and indoor wireless communication environments, such as: downtown areas, malls, airports, offices and laboratories. This includes modeling wireless channel of some popular wireless communication technologies that are currently available in the aforementioned areas, such as: wireless local area network (WLAN), wireless fidelity (Wi-Fi) and worldwide interoperability for microwave access (WiMAX) wireless communication systems. In this thesis, the development of a 3D geometrical scattering channel model for microcellular and picocellular outdoor and indoor wireless communication environments is presented..

1.3 Previous Work

In published literature, several 2D and 3D geometrical scattering channel models are currently available [16–40]. The 2D geometrical models provide the azimuth angular distributions, whereas the 3D models are able to describe both the azimuth and elevation angular distributions. For outdoor macrocellular wireless communication environments, where the BS antennas are elevated and the scatterers are assumed to be located around only the MS antennas various 2D [23, 24, 27–29, 31, 37, 38] and 3D [25, 30, 35, 40] geometrical scattering channel models have been developed. However, for microcellular and picocellular outdoor and indoor wireless communication environments, only 2D geometrical scattering channel models have been developed [16, 20, 22, 24, 33, 36].

Typically, in the later mentioned wireless communication environments, where the heights of the BS and the MS antennas and the distance between them are both relatively short in comparison to outdoor macrocellular environments. In such cases, the scatterers such as: roofs, walls, trees, doors, windows, the ground, etc., can be assumed to be available within a 3D space that includes both the BS and MS antennas. However, all the available geometrical channel models are 2D models, where the transmitted signal is assumed to propagate on the horizontal plane, i.e. the elevation angle is assumed to be 90°. For example, Liberti and Rappaport, in [16], developed the elliptical geometrical scattering channel model assuming that the scatterers are uniformly distributed on an ellipse where the BS and MS are located at it's foci. The marginal and joint probability density functions (pdfs) of the AOA and TOA are provided. In [20], Norklit, proposed a geometrical scattering channel model based on the assumption that the scatterers are distributed along circumferences of elevated ellipses, where the TOA variable is related to elevated BS antennas, but the AOA variable is based on distributing the scatterers on a 2D plane. The pdf of the AOA conditioned on the TOA variable is provided. Ertel and Reed, in [22], proposed a more general approach in which the pdfs for both the elliptical [16] and circular [23] geometrical scattering channel models can be derived using a common approach as seen from both the BS and the MS. In [24], Janaswamy, developed a Gaussian scatterer density model which assumed that the MS is surrounded by scatterers in a Gaussian distribution. The Gaussian model can be used in different wireless communication environments by changing the standard deviation of the scatterers around the MS. The pdf of the AOA, the pdf of the TOA, the power azimuth spectrum and the time delay spectrum can be estimated by this model. Jiang and Tan, in [33], developed a geometrical scattering channel model based on the assumption that the scatterers are randomly distributed around the BS within a circle that is determined by the coverage area of the BS antenna. The joint pdf of the AOA and TOA is derived for a general distribution of scatterers. Finally, Noor *et al.*, in [36], generalized the elliptical channel model for an arbitrary distribution of scatterers around the MS and/or the BS. The model assumes a Gaussian scatterers distribution around both the BS and MS, each with a different standard deviation. The pdf of the AOA is provided with consideration of two different scatterer distributions, i.e one around the BS and the other around the MS. However, all the pdfs of the AOA based on the aforementioned geometrical scattering channel models provide only the azimuth angular statistical distribution of the received multipath signals.

From a physical viewpoint, since the BS and MS antennas are low and the distance between them is small, then the scatterers are distributed within 3D space around and between both the BS and MS. Therefore, it is more reasonable to consider that the multipath signals propagate within both the azimuth, i.e. horizontal, and the elevation, i.e. vertical, planes. In addition, several outdoor and indoor channel measurements proved that the angular spread of the received multipath signals are observed within a relatively wide range of elevation angle in comparison to the 2D models' assumptions [41–45]. Consequently, the development of a 3D geometrical scattering channel model for later wireless communication environments is required.

1.4 Objectives

In this thesis, the objective is to develop a 3D geometrical scattering channel model for microcellular and picocellular outdoor and indoor wireless communication environments. Specifically, the model can be used in wireless communication environments, in which the most frequent occurrence of the AOA of the received multipath signals takes place around the relative direction of the BS to the MS in both the azimuth and elevation angles.

1.5 Contributions

The thesis outlines several noteworthy contributions to the area of geometrical scattering channel modeling techniques. In essence, the thesis' potential contributions are as follows:

- The development of a novel generalized 3D geometrical scattering channel model for wireless communication environments, where only 2D models are currently available. The model incorporates the spatial statistical distributions of the received multipath signals in both the azimuth and elevation angles [46].

- The verification of the developed 3D model by comparing its behavior against the results from a site-specific propagation prediction technique in indoor and outdoor wireless communication environments [46].
- The extension of the 3D geometrical scattering channel model in order to account for the TOA variable of the received multipath signals. In this case, both the spatial and temporal statistical distributions of the received multipath signals are included [47–49].
- The generalization of the extended 3D model for a general distributions of scatterers. As a case study, the 3D Gaussian scatterers density function is considered [50].
- The comparison of the proposed 3D model and its extended versions with the available similar geometrical scattering channel models. As special cases, the developed 3D models can be reduced to these geometrical scattering channel models.
- The development of a spatial correlation function that can be used in simulating and investigating MIMO wireless communication system performance [51].

1.6 Organization

The thesis is organized as follows. A background and literature review about the related topics are provided in Chapter 2. In Chapter 3, the new 3D geometrical scattering channel model's description, derivation of the pdfs of the AOA and their verification are provided. The extension of the developed 3D model for the inclusion of the TOA parameters is presented in Chapter 4, where the scatterers distribution is assumed to be uniform. In Chapter 5, the 3D model's extension for non-uniform scatterer distribution is provided, where the Gaussian scatterers distribution is assumed. The derivation, comparison and validation of the pdfs of the AOA and TOA are provided. The extension of the new 3D geometrical scattering channel for MIMO channel modeling is provided in Chapter 6. Derivation of the spatial correlation function of the received fading signals, as well as, it's application in simulating MIMO wireless performance is also provided. Finally, the conclusions and future work that can build upon the results of this thesis are given in Chapter 7.

Chapter 2

Background and Literature Review

2.1 Introduction

Satisfying the increasing demand for wireless communication services necessitates the efficient usage of the available wireless channel resources. The area of channel propagation resource utilization has attracted considerable attention in the last three decades. The channel resources which can be utilized include: frequency domain, i.e. frequency division multiple access (FDMA), time domain, i.e. time division multiple access (TDMA), power domain, i.e. code division multiple access (CDMA), and space domain, i.e. space division multiple access (SDMA). The basic concept of these different techniques is to allow for several users to simultaneously access a single communication channel. Multiple access wireless communication techniques have been developed for both fixed and mobile wireless service applications. However, wireless service providers are faced with a number of challenges, such as the limited availability of the radio frequency spectrum and the complexity time varying wireless communication channels, in addition to meeting the increasing demand for higher data rates,

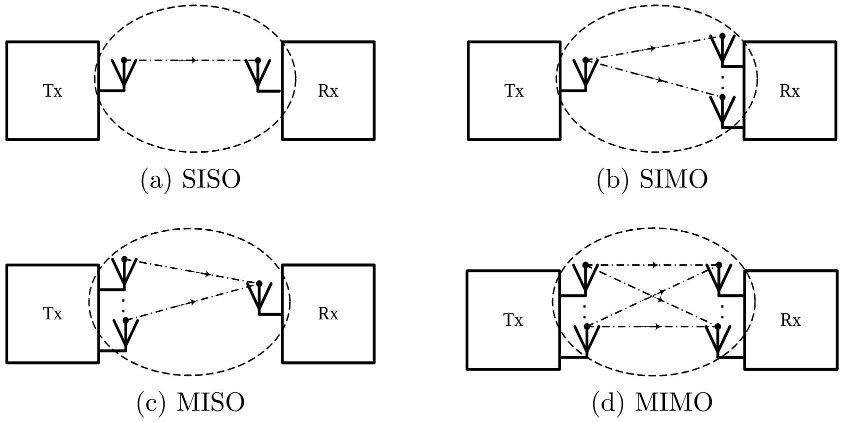

Figure 2.1: Antenna configuration in multiple antenna systems.

higher capacities, greater coverage areas and better quality of service. The use of MEA at the receiver (Rx) and/or at the transmitter (Tx) in wireless communication systems, which are commonly known as smart/adaptive antenna systems or space-time wireless communication systems, is an emerging technology that provides efficient utilization of the space domain.

2.2 Multiple Antenna Elements in Wireless Communication Systems

Figure 2.1 illustrates various antenna configurations for MEA wireless communication systems. As shown in Figure 2.1a, the SISO system is the most familiar wireless system and has only two antenna elements, one for transmitting and one for receiving. In multipath wireless communication environments, more than one antenna can be used at the transmitter and/or at the receiver to increase the signal to noise ratio (SNR) in order to improve the performance of wireless communication systems. For example, Figure 2.1b shows the configuration for SIMO wireless systems, i.e. receive diversity [1, 5], in such a case, the transmitter has only one antenna, whereas the receiver has more than one antenna. The received multipath signals at the receiver have different amplitudes and phases. Therefore, the receiver can coherently add the different multipath signals which are received by different antennas to enhance the quality of the signal. Similarly, in MISO wireless systems, i.e. transmit diversity, [6–8], the transmitter has more than one antenna, whereas the receiver has only one antenna, as shown in Figure 2.1c. In MISO systems, the transmitted signal can be sent by more than one antenna element. However, a suitable utilizing for the transmitted signal is required in order for the receiver to be able to extract the signals from multiple transmitter antennas, i.e. design of space-time codes. Generally the transmit and receive diversity can be characterized by the number of fading channels, which is known as diversity order. Figure 2.1d shows the MIMO system configuration. In such a system, both the transmitter and the receiver employ more than one antenna in order to utilize both receive and transmit diversity, which is known as spatial multiplexing. In this case, the diversity order is equal to the product of the number of transmitting and receiving antennas.

2.3 Multipath Wireless Propagation Environments

Transmitted signals propagate through wireless channels along a number of different paths. This results in scattering, diffraction and reflection of the transmitted signal by objects within the wireless medium, as shown in Figure 2.2. Therefore, the different propagation paths result in different delayed copies of the transmitted signal arriving at the receiver. These multipath signals can limit the performance of wireless communication systems by introducing intersymbol interference (ISI) and/or fading. When the difference in delays between the different multipath signals is large, i.e. large delay spread, the received data symbols might overlap. This leads to ISI at the receiver which can result in poor signal

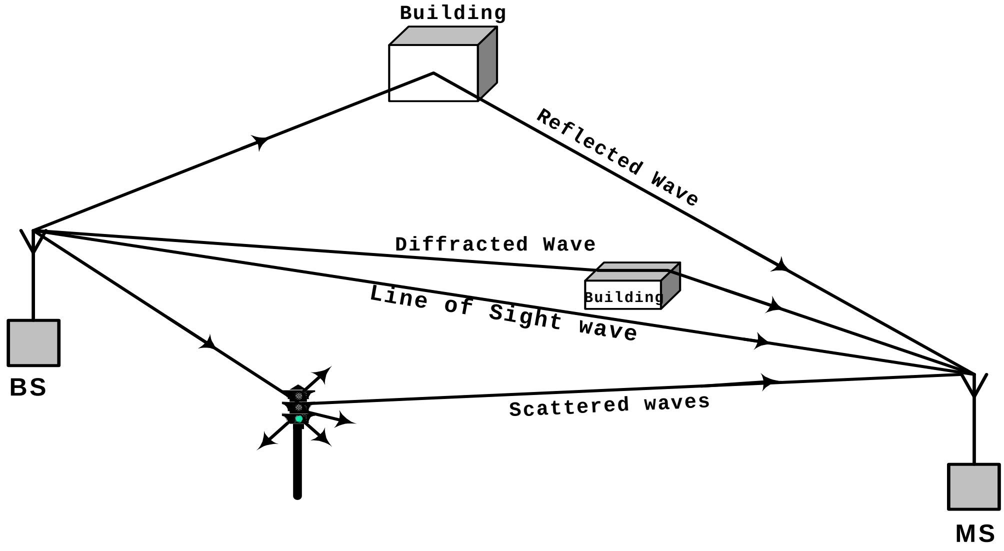

Figure 2.2: Wireless communication environment.

reception even when the signal level is high. Fading of the received signals can happen when the phases of the multipath signals combine destructively at the receiver even if the delay spread is low.

Furthermore, the angular spread can affect the quality of the received multipath signals. For example, it has been illustrated in [19, 52] that a wireless channel can be defined as a high rank channel, i.e. high capacity, if the delay spread, σ_τ, is equal to or larger than the inverse of the receiver bandwidth, B, or the angular spread, σ_Ω, is equal to or larger than the three decibel (3dB) beamwidth, Ω_{3dB}, of the antenna radiation pattern. Thus,

$$\sigma_\tau \geq \frac{1}{B} \qquad or \qquad \sigma_\Omega \geq \Omega_{3dB}. \tag{2.1}$$

On the other hand, the channel can be defined as a low rank channel if the delay spread, σ_τ, is small compared to the inverse of the receiver bandwidth, B, and the angular spread, σ_Ω, is small compared to the 3dB beamwidth, Ω_{3dB}, of the antenna radiation pattern. Thus,

$$\sigma_\tau \ll \frac{1}{B} \qquad or \qquad \sigma_\Omega \ll \Omega_{3dB}. \tag{2.2}$$

The angular spread, σ_Ω, of the received multipath signals depends on both the azimuth angular spread, σ_ϕ, and the elevation angular spread, σ_θ. Since the spatial and temporal correlation of the multipath signals can be limiting factors of wireless communication systems, the efficient exploitation of the angular and temporal dimensions can significantly enhance the systems performance. In order to exploit these dimensions efficiently, it is important to have reliable knowledge of the propagation characteristics of the transmission paths between the BS and MS in different wireless communication environments such as: macrocellular, microcellular, picocellular and indoor environments.

2.3.1 Macrocellular Environments

In macrocellular environments, i.e. a large cell, the BS covers several kilometers, i.e. the separation distance between the BS and the MS is several kilometers, and the BS antenna is usually elevated. In such cases, the height of the BS antenna is greater than the surrounding objects, therefore, it is reasonable to assume that the scatterers are distributed around only the MS. Since the distance between the BS and the MS is far greater in comparison to the difference between the heights of the BS/MS antennas, it is also reasonable to assume that the signal propagates within the horizontal plane. The macrocellular environments may include outdoor rural and urban areas.

2.3.2 Microcellular Environments

In microcellular environments, i.e. a smaller cell, the BS covers a few hundred meters to one kilometer and is able to provide increased capacity. In such cases, the typical heights of the BS and the MS antennas and the distance between them are both relatively short in comparison to macrocellular wireless environments. Therefore, the scatterers that cause multipath signals are assumed to be spread around both the BS and MS antennas. However, under some circumstances, the density of scatterers around the BS is less than the density of scatterers around the MS. Examples for microcellular environments are outdoor downtown areas.

2.3.3 Picocellular Environments

In picocellular environments, i.e. a very small cell, the distance between the BS and the MS is very small, i.e. several meters, and the BS/MS antennas are almost the same height. Therefore, in such cases, the scatterers can be assumed to be distributed around and between both the BS and MS antennas. Picocellular environments may include high traffic pedestrian areas, i.e. outdoor, and offices, i.e. indoor.

Typically, in macrocellular environments, the received signals express moderate values of angular spread and large values of delay spread, whereas in microcellular and picocellular environments the angular spread is high and the delay spread is low. Having both the spatial and temporal statistical information is useful in determining the performance of these wireless communication systems. It is possible to obtain the information from measured data or from site-specific propagation-prediction techniques, but this information is not always available and/or applicable. Therefore, channel models that are able of predicting the statistical distributions of received multipath signals are useful in characterizing the multipath wireless channels in different environments for different applications. Commonly used geometrical scattering channel models have been developed to obtain both the spatial and temporal statistical information of the multipath fading signals, as well as, the space-time correlation functions in various wireless communication environments.

2.4 Geometrical Scattering Channel Modeling Techniques

2.4.1 Definition

To evaluate the performance of a wireless communication system that employs antenna array, as well as, to investigate the properties of the received fading signals, geometrical scattering channel models have been developed. These models also known as single bounce scattering channel models, where the propagation between the transmitting and receiving antennas is assumed to take place via a single scattering from an intervening object, i.e. scatterer. The geometrical scattering channel models are based on the assumption that the scatterers that give rise to the multipath signals are randomly distributed within 2D or 3D space, and that space is assumed to be enclosed by a specified geometry that may include the BS and/or the MS antennas.

2.4.2 Assumptions

The following assumptions are commonly applied in geometrical scattering channel techniques in order to obtain convenient, simple statistical distributions for some of the physical quantities wireless channels.

- The transmission path from the transmitting antenna to the receiving antenna is assumed to happen via one scattering only, i.e. a single bounce multipath signal. Specifically, only significant scatterers that contribute to the last scatterering of the multipath received signals are considered. In other words, only scatterers that give rise to multipath signals which arrive at the receiver's side within a specified time and/or at specified power threshold values are considered, where these threshold values are determined by the system designer. The multiple scattering, i.e. multiple-bounce can be modeled in a further step as a stochastic process [4].

- The scatterers are assumed to be reflecting elements with equal scattering coefficients and uniform random phases. As mentioned before, the scatterers are assumed to be distributed within 2D or 3D space that is limited by a specific geometry which includes the BS and/or MS antennas. Unbounded scattering space can be used, i.e. without limiting geometry, but geometry has some advantages, such as: i) the ability to relate the derived statistical distributions to some of the important physical parameters, such as the distance between the BS and MS, ii) the ability to include only the most significant scatterers. The effects of the scatterers distributed outside the geometry can be ignored in comparison to the effects of the scatterers within the geometry. This assumption leads to obtain the necessary AOA and TOA pdfs in convenient forms.

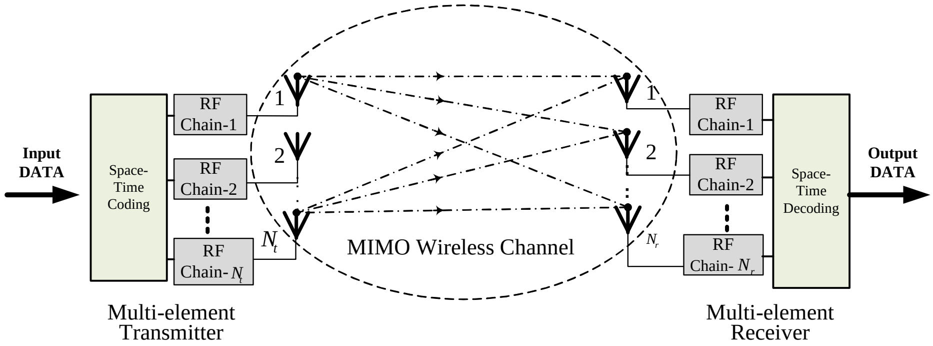

Figure 2.3: MIMO System.

- The employed antenna radiation patterns are isotropic for both the BS and MS. However, the actual antenna radiation pattern can be incorporated with the derived statistical distribution functions.

2.5 Multiple Input Multiple Output Wireless Systems

In a MIMO system, Multi-Element Antenna (MEA) structures are deployed at both the transmitter and receiver, as shown in Figure 2.3. From a communication engineering perspective, the challenge is to design the signals to be sent by the transmitter array, and the algorithms for processing those signals at the receiver array, so that the quality of the transmission, i.e. bit error rate, and/or its data rate are improved. These gains can then be used to provide increased reliability, lower power requirements, i.e. per transmit antenna, or higher composite data rates, i.e. either higher rates per user or more users per link. The benefits offered by MIMO technology is that these improvements can be obtained without the need for additional spectral resources. The MIMO system over a realistic wireless channel has been developed theoretically [12, 14, 15] and demonstrated experimentally, [12, 13] as long as the environment provides sufficient scattering, i.e. a rich multipath environment. It has been shown that the MIMO capacity can linearly increases with the minimum number of antenna elements N, where $N \leq \min(N_t, N_r)$, where N_t and N_r are the number of antenna elements at the transmitter and the receiver, respectively. In general, a MIMO channel represents N parallel sub-channels, such that the MIMO capacity is the sum of the individual capacities of the sub-channels. The MIMO system's capacity has been derived as

$$C = \ln \det(I_{N_r} + \frac{SNR}{N_t} HH^T), \tag{2.3}$$

where I_{N_r} is $N_r \times N_r$ identity matrix, SNR is the average signal-to-noise ratio (SNR), H is the $N_r \times N_t$ complex fading envelopes, $(.)^T$ denotes the transpose conjugate, and $\det(.)$ denotes the matrix determinant. The performance of MIMO systems can be maximized when the channel transfer matrix is full rank. This can be achieved when there is no correlation or at least the correlation is low between the various transmitted signals, as well as, the various received signals. In an antenna array system such as MIMO, there are two main sources of correlation. The first one is a non-rich scattering environment, where the multipath components arrive at the receiver within a limited direction in space. The other correlation source is the mutual coupling between the antenna elements employed. Therefore, in order to understand the behavior of a MIMO system, a better channel model is required for the purpose of assisting in the design of an efficient MIMO system. This model should take into account the spatial information of the received multipath signals, as well as, the employed antenna array properties.

2.6 Multiple Input Multiple Output Channel Modeling

Typically, wireless channel conditions and the type of antenna array employed at both the transmitter and the receiver have an influence on the performance of MIMO wireless systems. Hence, it becomes essential to model a radio channel which includes the effects of the MIMO radio channel and the antenna that is employed. Since the MIMO performance is limited by the correlation between the various signals that are received by the different antenna elements, it is important to model the correlation in order to achieve the maximum performance of the wireless MIMO system. Therefore, the geometrical scattering channel modeling technique have been suggested to obtain the spatial correlation function of the received multipath fading signals, as well as, describe the MIMO wireless transfer function, H. This technique can lead to obtain a simple correlation function and taking into account some important channel physical parameters's. In the last few years, considerable research has been devoted to modeling the channel and correlations, along with performance analysis of the MIMO wireless systems based on geometrical scattering channel modeling technique, see for example, [53–58].

2.7 Literature Review

As mentioned before, geometrical scattering channel models have been developed for both the conventional wireless systems, i.e. SIMO, to describe the AOA and TOA statistical distribution and MIMO wireless systems to describe the spatial correlation functions. For example conventional wireless systems several geometrical scattering channel models have been developed for different types of environments. In macrocellular environments, many 2D [23, 24, 27, 29, 31, 37, 38] and 3D [25, 30, 35, 40] geometrical scattering channel models are currently available. The circular geometrical scattering channel model, where the scatterers are assumed to be uniformly distributed within a circle around the MS, has been suggested in [3], as shown in Figure 2.4a. The marginal and joint pdfs of the AOA and TOA have been obtained as seen from the BS and MS. For example, the joint AOA and TOA is given by [3]

$$f(\tau, \phi_m) = \frac{(D^2 - \tau^2 c^2)(D^2 c - 2D\tau c^2 \cos\phi_m + \tau^2 c^3)}{4\pi R^2 (D\cos\phi_m - \tau c)^3}, \qquad \tfrac{D^2 - 2\tau c^2 \cos\phi_m + \tau^2 c^2}{\tau c - D\cos\phi_m} \leq 2\,R, \tag{2.4}$$

where D, R, c, τ, and ϕ_m are, respectively, the distance between the BS and the MS, radius of the circle, speed of light, TOA of the multipath signals, and AOA of the multipath signals in the azimuth plane. In order to describe the angular spread in both the azimuth and the elevation angles in macrocellular environments, some 3D geometrical scattering channel models have been suggested. For example, in [25], Janaswamy developed a 3D spheroid model. This based on the assumption that the scatterers are uniformly distributed within the upper half of a spheroid and the MS antenna is located at its center, as shown in Figure 2.4b. The author provided closed form expressions for the joint and marginal pdfs of the AOA as seen from the BS and MS. For example, the provided joint pdf of the AOA as seen from the MS is given by [25]

$$f(\theta_m, \phi_m) = \frac{a\, b^2 \cos\theta_m}{2\pi \left(b^2 \, \sin^2\theta_m + a^2 \cos^2\theta_m\right)^{3/2}}, \tag{2.5}$$

$$0 < \theta_m \leq \pi/2, \quad 0 < \phi_m \leq 2\pi,$$

where a, b, are the spheroid's semi-lengths on the major axes, i.e. x and y-axes, and minor axis, i.e. z-axis, respectively and θ_m and ϕ_m are respectively, the AOA of the multipath

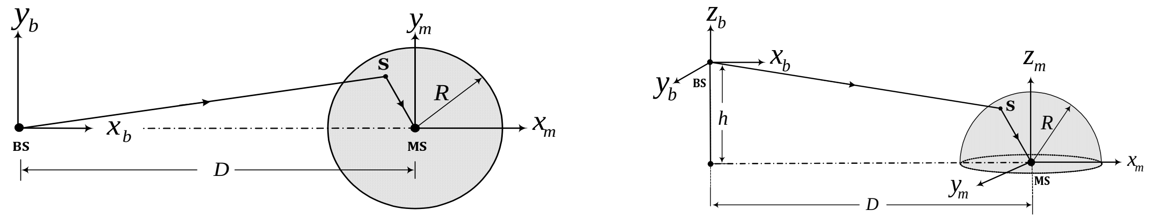

(a) 2D circular model (b) 3D spheroid model

Figure 2.4: Geometrical scattering channel models for macrocellular environments: a) Circular model and b) Spheroid model.

signals in the elevation and the azimuth angle.

In microcellular and picocellular outdoor environments and indoor wireless communication environments, several geometrical scattering channel models are currently available [16, 20, 22, 24, 33, 36]. However, all the available geometrical channel models are 2D models, where the transmitted signal is assumed to propagate on the horizontal plane, i.e. the elevation angle is assumed to be 90°. In other words, the 2D models are capable of predicting only the angular information in the azimuth plane. The first 2D geometrical scattering channel model that was developed for the previously mentioned environments is the elliptical model [16]. Liberti and Rappaport, developed this model based on assuming that the scatterers are uniformly distributed inside an ellipse in which the BS and the MS are located at its foci, as shown in Figure 2.5a. Expressions the marginal, joint, and conditioned pdfs of the AOA and TOA of the received multipath signals are provided. For example, the joint pdf of the AOA and TOA is obtained as

$$f(\tau, \phi_m) = \frac{(D^2 - \tau^2 c^2)(D^2 c - 2D\tau c^2 \cos\phi_m + \tau^2 c^3)}{4\pi a\, b(D\cos\phi_m - \tau c)^3}, \qquad \tfrac{D}{c} < \tau < \tau_m. \tag{2.6}$$

To include the relative difference between the BS and MS antennas, Norklit in [20], proposed

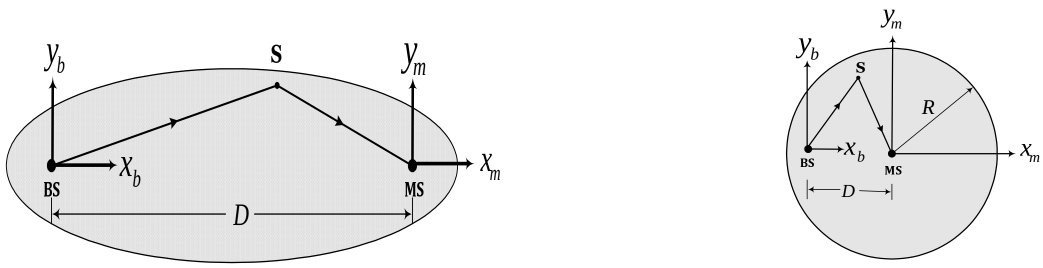

(a) 2D elliptical model (b) 2D circular model

Figure 2.5: Geometrical scattering channel models for microcellular and picocellular outdoor and indoor environments: a) Elliptical model and b) Circular model .

a geometrical scattering channel model based on the assumption that the scatterers are distributed along circumferences of several elevated ellipses, where the TOA variable is related to elevated BS antennas, but the AOA variable is based on distributing the scatterers on a 2D plane, i.e. ellipse surface. The marginal pdf of the AOA conditioned on the TOA variable is provided and the pdf captures only the azimuthal angular information. In [22], Ertel and Reed, proposed a more general approach in which the pdfs for both the elliptical [16] and circular [23] geometrical scattering channel models can be derived as seen from both the BS and the MS sides. Janaswamy, in [24], developed a Gaussian scatterer density model which assumes that the MS is surrounded by the scatterers in a Gaussian distribution, which was an extension of the circular model for a non-uniform scatterers distribution. Janaswamy's model can be used in different wireless communication environments by changing the standard deviation of the scatterers around the MS. Expressions for the marginal pdfs of the AOA and TOA, the power azimuth spectrum and the time delay spectrum are provided. Expressions are also provided for some of the quantities of practical interest such as the root mean square (RMS) angular spread, the RMS delay spread, and the spatial correlation function. The Gaussian scatterers density model has been validated by comparing the AOA and TOA pdfs with the circular [23] and the elliptical geometrical scattering channel models [16], as well as, with some available channel measured data for outdoor and indoor environments.

Jiang and Tan, in [33], developed a geometrically based statistical channel model with scatterers that are randomly distributed around the BS within a circle that is determined by the coverage area of the BS antenna, as shown in Figure 2.5b. The marginal and joint pdfs of the AOA and TOA are provided for a general distribution of scatterers around the BS. As special cases, Rayleigh and exponential scatterers distributions are investigated. Comparison results of Jiang's model with some of the available measured data show that the Rayleigh scatterer distribution model can be applied to outdoor microcellular environments, whereas the exponential scatterer distribution model gives accurate results for an indoor office/laboratory wireless environment. Finally, Noor *et al.*, in [36], generalized the elliptical channel model for an arbitrary distribution of scatterers around the MS and/or the BS. The model is based on assuming a Gaussian scatterers distribution around both the BS and MS, each with a different standard deviation. The marginal pdf of the AOA is provided, where two different scatterer distributions are considered, i.e one around the BS and the other around the MS. Also, the pdf has been compared with some of the available measured data in both indoor and outdoor environments.

For MIMO case, several geometrical scattering channel models are currently available [53–58]. Shiu *et al.* in [53], investigated the effects of fading correlations on the performance of MIMO communication systems. Their model is based on the assumption that the scatterers are uniformly distributed on a ring around the MS, i.e. one-ring model. An expression for the spatial correlation function of the received multipath fading signals was obtained and shows that the fading correlation depends on the physical parameters of MIMO and the characteristics of the scatterer. In [54] Abdi *et al.* generalized the one-ring model to provide the space-time cross correlation function for mobile frequency nonselective Rican fading MIMO channels. This model is based on the assumption that the scatterers are distributed according to von Mises density function [54]. The model includes various parameters of interest, such as the angular spread at the BS and MS, the distance between the BS and MS, mean directions of the signal arrivals, array configurations, and Doppler spread. Byers *et al.*, in [55], extended the one-ring model to include the scatterers around both the BS and the MS. The model provides the space-time correlation function, where the scatterers are assumed to be distributed on two rings around the BS and the MS, i.e. two-ring model. Similarly, they assumed the scatterers were distributed according to the von Mises density function. Chen *et al.*, in [56], developed two models to obtain the spacetime correlation functions of fading signals for both frequency-flat and frequency-selective channels in both macrocellular and microcellular environments. For the macrocellular, the scatterers are assumed to be uniformly distributed inside a circular ring around the MS. For the microcellular, the scatterers are assumed to be distributed inside an elliptical ring enclosing both the BS and the MS. In the 3D case, the one-ring and the two ring models have been extended, in [57, 58], to include the elevation angular spread information. In [57], Gong *et al.*, assumed that the scatterers are uniformly distributed over a sphere, where the MS at is its center. Zajic *et al.*, in [58], developed an extension for the two-ring model by assuming that the scatterers are distributed on the surface of two cylinders around both the BS and the MS. They assumed that the scatterers are distributed in the azimuth and elevation plane based on the von Mises density function, and the cosine function, respectively.

In this thesis, a new 3D geometrical scattering channel model has been developed for microcellular and picocellular outdoor environments and indoor wireless communication environments, where only 2D model is currently available in literature. [46–51]. This model can be used to describe the angular and temporal statistical distributions of the received multipath signals as seen from both the transmitter and the receiver sides, as well as, the spatial correlation functions. In [46], the new geometrical model, i.e. the ellipsoidal model, have been developed and verified. The marginal and joint pdfs of the AOA are provided in compact forms and facilitate independent control of the angular spread in both the azimuth and the elevation angles via the model's parameters. To include the TOA of the multipath signals, a new 3D geometrical scatterering channel, i.e the spheroid model, model have been developed for uniform scatterers distributions [47–49]. In this case, several pdfs of the AOA and TOA are provided, such as: the marginal and joint pdfs of the AOA, the joint pdfs of the AOA conditioned on the TOA and the marginal pdf of the TOA. The pdfs of the AOA have been validated by compare them with similar 2D models which available in literature. For non-uniform scatterers distribution, the 3D spheroid model has been generalized for an arbitrary distribution of the scatterers In [46]. The joint pdfs of the AOA and TOA are provided and validated by comparing them with channel measured data. All the pdfs of the AOA can be expressed as seen from both the transmitter and the receiver sides. For MIMO channel modeling applications, a new 3D spatial correlation function has been developed [51]. This function is based on extending the new 3D ellipsoid model to obtained the correlation coefficients between various transmit and receive fading signals. Several numerical examples for MIMO systems' performance have been provided based on the spatial correlation functions.

Chapter 3

Angle of Arrival Statistics for a Three Dimensional Geometrical Scattering Channel Model

3.1 Introduction

In this chapter, a 3D geometrical scattering channel model is introduced. The model is based on the assumption that the scatterers are uniformly distributed inside an ellipsoid volume, in which the BS and the MS are placed at the ellipsoid's foci, i.e. the 3D ellipsoidal model. The joint pdf of the AOA of the received multipath signals are provided. The derived pdf facilitates independent control of the angular spread in both the azimuth and elevation angles via the model's parameters. The developed 3D ellipsoidal model has been verified by comparing the derived pdfs against the results from a site-specific propagation prediction technique applied to indoor and outdoor wireless communication environments.

3.2 Model's Description

The model's geometry is shown in Figure 3.1. The ellipsoid is centered at O which is the origin of the Global Cartesian coordinate system (x_g, y_g, z_g). The MS and BS antennas are

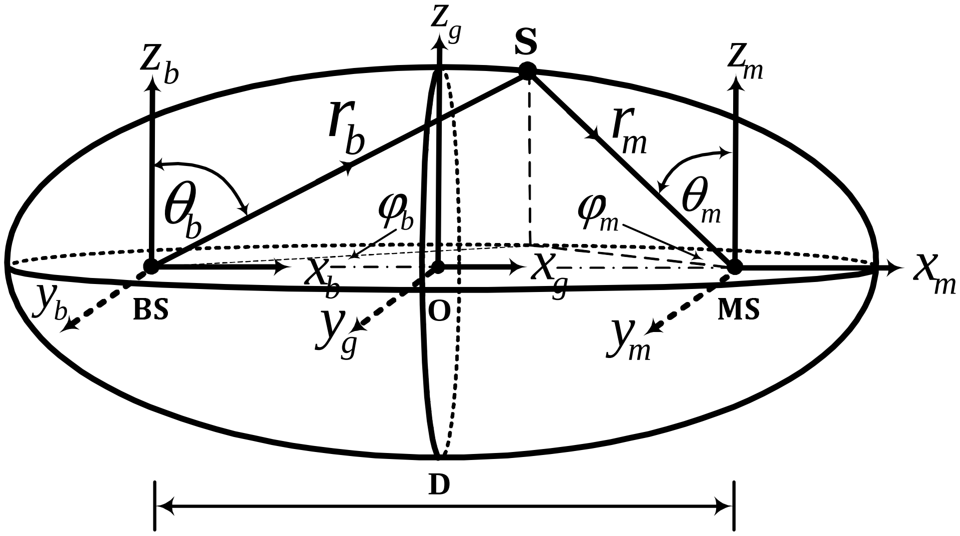

Figure 3.1: Ellipsoidal model's geometry.

located on the x-axis at the ellipsoid's foci $(\pm f, 0, 0)$ and separated by a distance of $D = 2f$, where f is the ellipsoid's focal length. The scatterers are uniformly distributed within the ellipsoid's volume, but for graphical simplicity, the figure shows only one scatterer denoted by **S**. The scatterer's Cartesian and Spherical coordinates with respect to the MS location are (x_m, y_m, z_m) and (r_m, θ_m, ϕ_m), respectively, while those with respect to the BS locations are (x_b, y_b, z_b) and (r_b, θ_b, ϕ_b). The transformation relationships between these various coordinate systems are given by:

$$x_g = D/2 + x_m = -D/2 + x_b, \qquad x_m = r_m \sin\theta_m \cos\phi_m, \quad x_b = r_b \sin\theta_b \cos\phi_b, \tag{3.1}$$

$$y_g = y_m = y_b, \qquad y_m = r_m \sin\theta_m \sin\phi_m, \quad y_b = r_b \sin\theta_b \sin\phi_b, \tag{3.2}$$

$$z_g = z_m = z_b, \qquad z_m = r_m \cos\theta_m, \qquad z_b = r_b \cos\theta_b. \tag{3.3}$$

Therefore, the ellipsoid can be described by any of the following formulas

$$\frac{x_g}{a^2} + \frac{y_g}{b^2} + \frac{z_z}{c^2} = 1.0, \tag{3.4}$$

$$\frac{(D/2 + r_m \sin\theta_m \cos\phi_m)^2}{a^2} + \frac{r_m^2 \sin^2\theta_m \sin^2\phi_m}{b^2} + \frac{r_m^2 \cos^2\theta_m}{c^2} = 1.0, \tag{3.5}$$

$$\frac{(-D/2 + r_b \sin\theta_b \cos\phi_b)^2}{a^2} + \frac{r_b^2 \sin^2\theta_b \sin^2\phi_b}{b^2} + \frac{r_b^2 \cos^2\theta_b}{c^2} = 1.0, \tag{3.6}$$

where a, b, and c are the ellipsoid's semi-lengths on the major axis, i.e. x-axis, and minor axes, i.e. y and z-axis, respectively, and (θ_m, ϕ_m) and (θ_b, ϕ_b) are the AOA of the multipath signals in the elevation and azimuth angles as seen from both the MS and BS, respectively. Simplifying (3.5) and (3.6) and solving for r_m and r_b results in new formulas that are capable of describing the ellipsoid in the Spherical coordinate system as seen from its foci. This yields

$$r_m = \frac{2b^2 c}{\left(2a\sqrt{c^2 \sin^2\theta_m + b^2 \cos^2\theta_m} + c\,D \sin\theta_m \cos\phi_m\right)}, \tag{3.7}$$

and

$$r_b = \frac{2b^2 c}{\left(2a\sqrt{c^2 \sin^2\theta_b + b^2 \cos^2\theta_b} - c\,D \sin\theta_b \cos\phi_b\right)}. \tag{3.8}$$

The ellipsoid's geometrical parameters are related to the BS/MS separation distance, D, as given by

$$
\begin{aligned}
a &= \frac{D}{2e_1}, && && (3.9)\\
b &= a\sqrt{1-e_1^2}, && 0 < e_1 < 1.0, && (3.10)\\
c &= a\sqrt{1-e_2^2}, && 0 < e_2 < 1.0, && (3.11)
\end{aligned}
$$

where e_1 and e_2 are the ellipsoid's eccentricities in the xy and xz planes respectively.

3.3 Angle of Arrival Probability Density Functions

The objective of this chapter is to derive the AOA pdf of the received multipath signals as seen from both the MS and the BS sides. Since the scatterers are uniformly distributed inside the ellipsoid's volume V, where $V = 4\,\pi\,a\,b\,c/3$, then the scatterers density function in the Cartesian coordinate systems with respect to the MS is given by

$$f(x_m, y_m, z_m) = \frac{3}{4\,\pi\,a\,b\,c}. \tag{3.12}$$

The corresponding scatterers density function in the Spherical coordinate system is obtained by using the Jacobian transformation. Hence,

$$f(r_m, \theta_m, \phi_m) = \left. \frac{f(x_m, y_m, z_m)}{|J(x_m, y_m, z_m)|} \right|_{\substack{x_m = r_m \sin\theta_m \cos\phi_m, \\ y_m = r_m \sin\theta_m \sin\phi_m, \\ z_m = r_m \cos\theta_m,}} \tag{3.13}$$

where $J(x_m, y_m, z_m)$ is the Jacobian transformation that is given by

$$J(x_m, y_m, z_m) = \begin{vmatrix} \frac{\partial x_m}{\partial r_m} & \frac{\partial x_m}{\partial \theta_m} & \frac{\partial x_m}{\partial \phi_m} \\ \frac{\partial y_m}{\partial r_m} & \frac{\partial y_m}{\partial \theta_m} & \frac{\partial y_m}{\partial \phi_m} \\ \frac{\partial z_m}{\partial r_m} & \frac{\partial z_m}{\partial \theta_m} & \frac{\partial z_m}{\partial \phi_m} \end{vmatrix}^{-1} = \frac{1}{r_m^2 \sin\theta_m}. \tag{3.14}$$

Therefore, the scatterers density function in the Spherical and the Cartesian coordinate systems can be related as given

$$f(r_m, \theta_m, \phi_m) = r_m^2 \sin\theta_m f(x_m, y_m, z_m). \tag{3.15}$$

By integrating (3.15) with respect to r_m, and substituting (3.7) and (3.12) into the result, the AOA joint pdf at the MS can be derived as

$$f(\theta_m, \phi_m) = \frac{2b^5 c^2 \sin\theta_m}{\pi a \left(2a\sqrt{b^2 \sin^2\theta_m + c^2 \cos^2\theta_m} + cD \sin\theta_m \cos\phi_m\right)^3}$$
$$0 < \theta_m \leq \pi \;, \quad 0 < \phi_m \leq 2\pi. \tag{3.16}$$

The derived AOA joint pdf can be obtained in terms of the ellipsoid's eccentricities as given

$$f(\theta_m, \phi_m) =$$
$$\frac{(1-e_1^2)^{5/2}\,(1-e_2^2)\sin\theta_m}{4\pi\left(\sqrt{(1-e_2^2)\sin^2\theta_m + (1-e_1^2)\cos^2\theta_m} + e_1\sqrt{1-e_2^2}\sin\theta_m\cos\phi_m\right)^3}$$
$$0 < \theta_m \leq \pi \;, \quad 0 < \phi_m \leq 2\pi, \tag{3.17}$$

where $e_1 = D/2a = \sqrt{1-(b/a)^2}$ and $e_2 = \sqrt{1-(c/a)^2}$. The marginal pdf in the azimuth and the elevation planes may be obtained in convenient forms for numerical evaluation as

$$f(\theta_m) \;=\; \int_0^{2\pi} f(\theta_m, \phi_m)\, d\phi_m \,, \quad 0 < \theta_m \leq \pi. \tag{3.18}$$

and

$$f(\phi_m) \;=\; \int_0^{\pi} f(\theta_m, \phi_m)\, d\theta_m \,, \quad 0 < \phi_m \leq 2\pi. \tag{3.19}$$

Similarly, the AOA joint pdf at the BS can be obtained by using (3.8) and following the previous procedures. This gives

$$f(\theta_b, \phi_b) = \frac{2b^5 c^2 \sin\theta_b}{\pi a \left(2a\sqrt{b^2\,\sin^2\theta_b + c^2\cos^2\theta_b} - cD\sin\theta_b\cos\phi_b\right)^3},$$
$$0 < \theta_b \leq \pi \;,\quad 0 < \phi_b \leq 2\pi. \tag{3.20}$$

3.4 Model's Comparisons

The proposed 3D geometrical scattering channel model can be used to deduce some previously proposed 2D and 3D models that assume uniform distribution of scatterers for outdoor and indoor wireless environments.

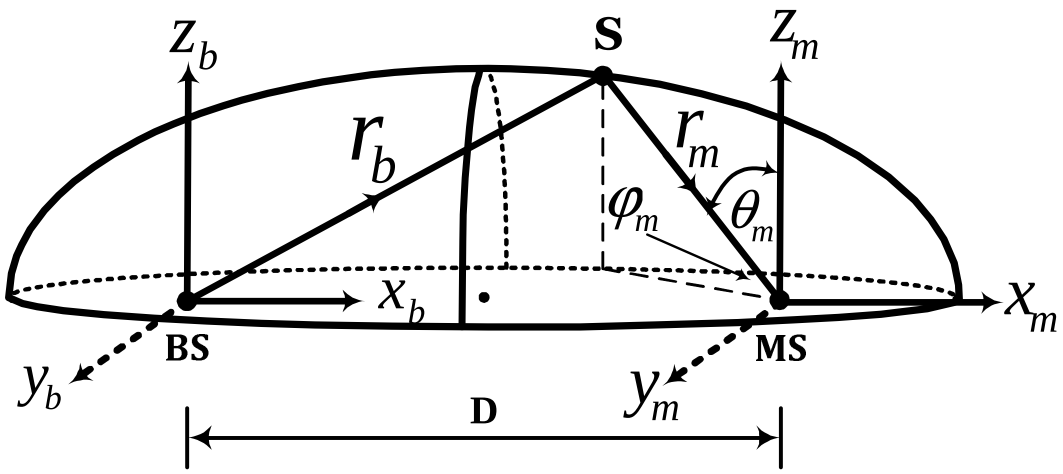

Figure 3.2: Hemispheroid model's geometry.

3.4.1 Three Dimensional Hemispheroid Model

Janaswamy, in [25], developed the 3D hemispheroid channel model for macrocellular wireless environments, where the scatterers are uniformly distributed around only the MS within a hemispheroid volume. The developed 3D ellipsoidal model can be used to extend Janaswamy's model to include the scatterers around and between both the BS and the MS by reducing the ellipsoid geometry to hemispheroid geometry, i.e. $0 < \theta_m \leq \pi/2$, as shown in Figure 3.2. The joint pdf of the AOA may obtained as

$$f(\theta_m, \phi_m) = \frac{4\, b^5 c^2 \sin\theta_m}{\pi a \left(2a\sqrt{c^2\, \sin^2\theta_m + b^2\cos^2\theta_m} + cD\sin\theta_m\cos\phi_m\right)^3},$$

$$0 < \theta_m \leq \pi/2\ , \quad 0 < \phi_m \leq 2\pi. \tag{3.21}$$

As a special case, the AOA joint pdf, in [25], at the MS is obtained by substituting $D = 0$ and $a = b$ into (3.21), and using the polar angle θ_m, rather than the author's assumption $\pi/2 - \theta_m$. In such case, the scatterers are assumed to be distributed within hemispheroid around the MS only, i.e. the MS is located at it's center. This yields

$$f(\theta_m, \phi_m) = \frac{a\, c^2 \sin\theta_m}{2\pi \left(c^2\, \sin^2\theta_m + a^2 \cos^2\theta_m\right)^{3/2}}, \tag{3.22}$$

$$0 < \theta_m \leq \pi/2, \quad 0 < \phi_m \leq 2\pi,$$

which is exactly the same as equation (9) of [25], where a and b are the spheroid semi-lengths on the major axes, i.e. x and y-axes and minor axis, i.e. z-axis, respectively.

3.4.2 Three Dimensional Spheroid Model

The 3D spheroid channel model has been developed in [46–48]. The model is based on the assumption that the scatterers are uniformly distributed within a spheroid volume. The 3D ellipsoidal model can be used to obtain the spheroid model by assuming that the ellipsoid's eccentricities in the xy and xz planes are equal. Therefore, by substituting $b = c$ into (3.16) or $e_1 = e_2 = e$ into (3.17), the AOA joint pdf can be obtained as

$$f(\theta_m, \phi_m) = \frac{2b^4 \sin\theta_m}{\pi a \left(2a + D \sin\theta_m \cos\phi_m\right)^3}, \qquad 0 < \theta_m \leq \pi \;, \quad 0 < \phi_m \leq 2\pi, \tag{3.23}$$

or

$$f(\theta_m, \phi_m) = \frac{(1 - e^2)^2 \sin\theta_m}{4\pi(1 + e \sin\theta_m \cos\phi_m)^3}, \qquad 0 < \theta_m \leq \pi \;, \quad 0 < \phi_m \leq 2\pi, \tag{3.24}$$

which has been derived based on the spheroid model, as detailed in Chapter 4.

3.4.3 Two Dimensional Elliptical Model

The well known 2D elliptical scattering channel model has been developed in previous literature for microcellular and picocellular outdoor wireless environments. The model is based on the assumption that the scatterers are uniformly distributed within an ellipse, where the BS and the MS are located at its foci [3, 16, 20, 22]. The generalized 3D model can also be used to obtain the marginal AOA pdf in the azimuth plane, where the propagation is assumed to take place within the horizontal plane, i.e. $\theta_m = 90^o$. In this case, substituting $\theta_m = 90^o$ and $e_2 = 0$ into (3.7) results in the 2D radial distance that can be used to describe the ellipse from its foci as given

$$r_m = \frac{a\,(1-e^2)}{(1+e\ \cos\phi_m)}. \tag{3.25}$$

This formula can be used to obtain the AOA marginal pdf as shown by

$$f(\phi_m) = \frac{(1-e^2)^{3/2}}{2\pi(1+e\cos\phi_m)^2}, \tag{3.26}$$

which is exactly the same as the AOA marginal pdf in the azimuth plane that is given in [3, 16, 20, 22]

3.5 Numerical Results and Model's Verifications

In order to illustrate and to verify the proposed 3D channel model, several 2D and 3D numerical plots for the new derived pdfs are provided. Figure 3.3a and Figure 3.3b show the 3D plot of the AOA joint pdfs as seen from the MS, $f(\theta_m, \phi_m)$, and the BS, $f(\theta_b, \phi_b)$, for the ellipsoid with eccentricities of $e_1 = 0.75$ and $e_2 = 0.90$. As illustrated in the figures, all the

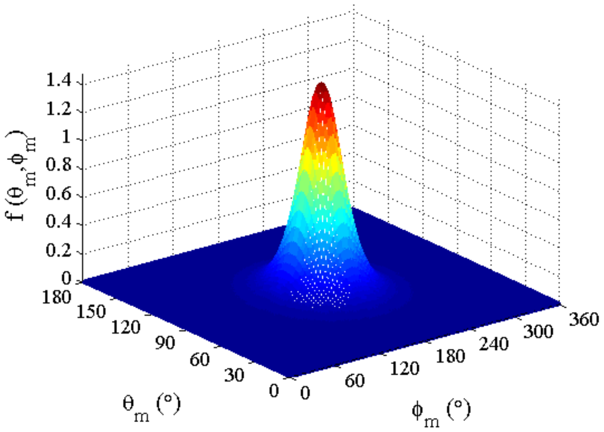

(a) $f(\theta_m, \phi_m)$

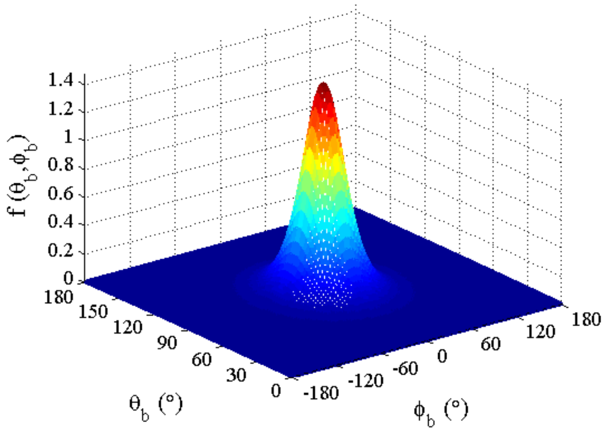

(b) $f(\theta_b, \phi_b)$

Figure 3.3: The joint pdfs of the AOA as seen from the MS and the BS, for e_1 = 0.75 and e_2 =0.90.

curves show that the most frequent occurrences of the signals' AOA take place around the relative direction of the MS to the BS in both the azimuth plane, $\phi_m = 180^o$, $\phi_b = 0^o$, and the elevation plane $\theta_m = 90^o$, $\theta_b = 90^o$.

To verify the derived pdfs, histogram simulations were used. The histogram simulations were created by distributing 200,000 scatterers uniformly within an ellipsoid. Then, the desired AOA for each scatterer was determined as seen from both the MS and the BS. The simulated AOA data was used to create histograms containing 50 bins, i.e. intervals. The number of points in each bin was normalized to the total number of points in order to generate simulated pdfs. Figure 3.4a and Figure 3.4b, respectively, show the plots of the theoretical and histogram simulations of the AOA pdf in the azimuth angle versus e_1 and in the elevation angle versus e_2 at a fixed value of e_1. Note that the angular spread in the azimuth angle depends only on the parameter of e_1, whereas the angular spread in the elevation angle depends on both parameters e_1 and e_2. Clearly, all the plots illustrate

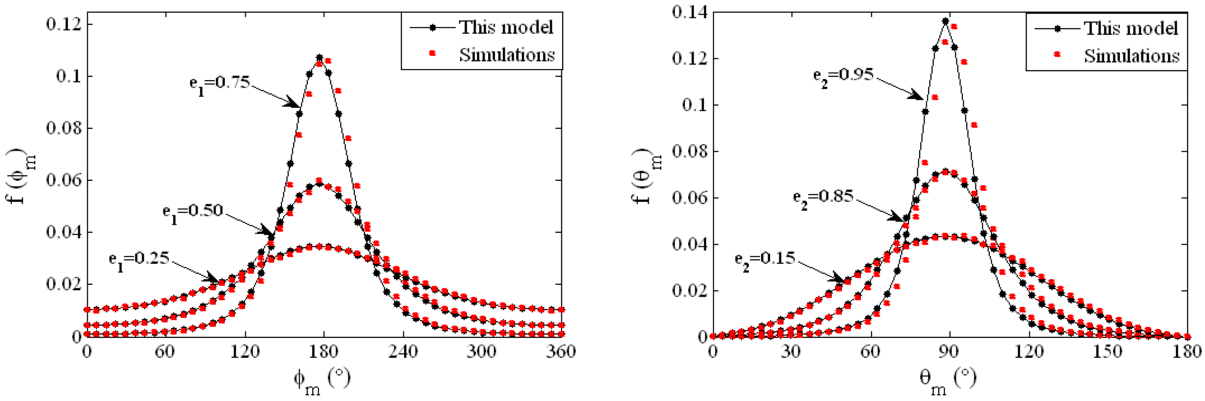

(a) $f(\phi_m)$

(b) $f(\theta_m)$

Figure 3.4: Comparison of the theoretical AOA marginal pdf with histogram simulations, at the MS: a) In the azimuth angle at different values of e_1, where $e_2 = 0.50$, and b) In the elevation angle at different values of e_2, where $e_1 = 0.85$.

that the most frequent occurrences of the AOA take place around the relative direction between the MS to the BS. Also, the larger the ellipsoid's size, i.e. smaller values of e_1 and e_2, the larger the angular spread in the elevation and the azimuth planes. All curves show good agreement between the theoretical and the histogram simulation results. The azimuth and elevation AOA marginal pdf plots, as seen from the BS, are shown in Figure 3.5a and Figure 3.5b, respectively. The plots illustrate a similar behavior for the pdfs as seen from the MS, which is expected, since the model's geometry is symmetrical as seen from both sides and the scatterers are assumed to be distributed uniformly. One advantage of having a 3D model is the ability to investigate the behavior of the AOA pdf in various planes. For example, the AOA pdf in the azimuth plane is illustrated in Figure 3.6a for different values of the elevation angle, θ_m, while the AOA pdf in the elevation plane for different values of the azimuth angle, ϕ_m, is shown in Figure 3.6b.

To establish a verification of the proposed model, the AOA pdfs have been compared against simulated results from a site-specific propagation prediction, i.e. ray-tracing, tech-

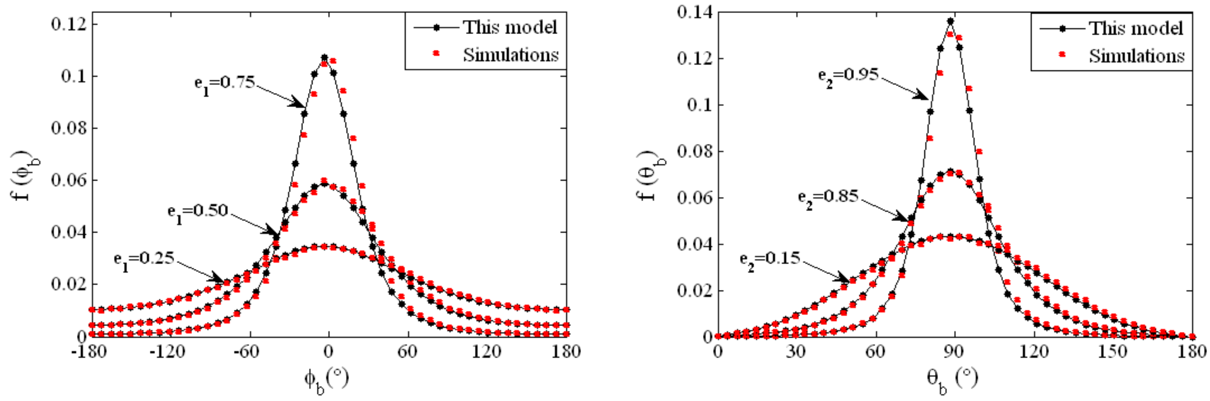

(a) $f(\phi_b)$ (b) $f(\theta_b)$

Figure 3.5: Comparison of the theoretical AOA marginal pdf with histogram simulations, at the BS: a) In the azimuth angle at different values of e_1, where $e_2 = 0.50$, and b) In the elevation angle at different values of e_2, where $e_1 = 0.85$.

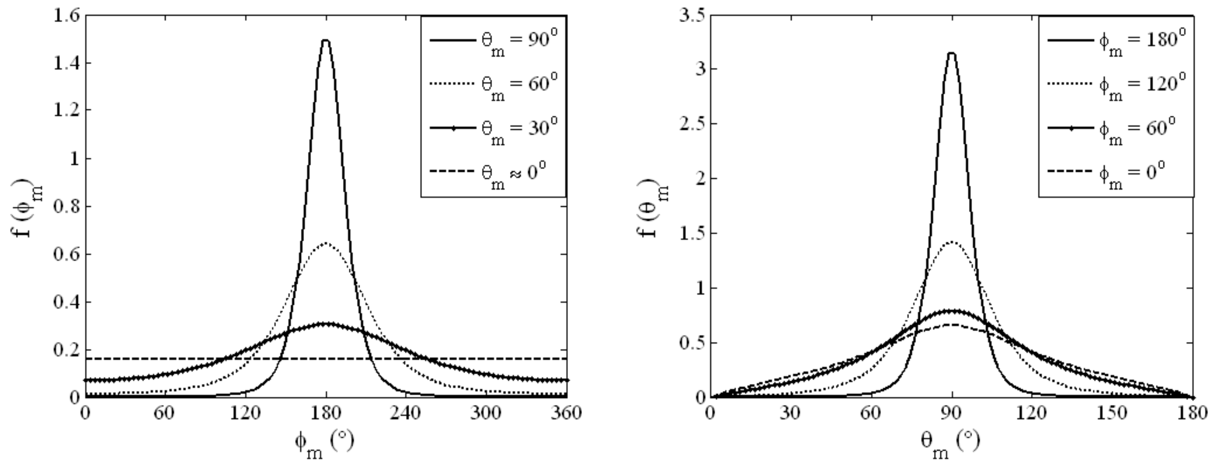

(a) $f(\phi_m)$ (b) $f(\theta_m)$

Figure 3.6: The AOA pdf for different planes, a) The AOA pdf in the azimuth angle $f(\phi_m)$ for different values of θ_m, b) The AOA pdf in the elevation angle $f(\theta_m)$ for different values of ϕ_m.

nique. The simulations were performed using the commercially available Wireless InSite software package [59]. The software has been used to model indoor and outdoor wireless communication environments, as shown in Figure 3.7 and Figure 3.8, respectively. To generate sufficient multipath signals, 100 receivers were placed at separate locations. This number

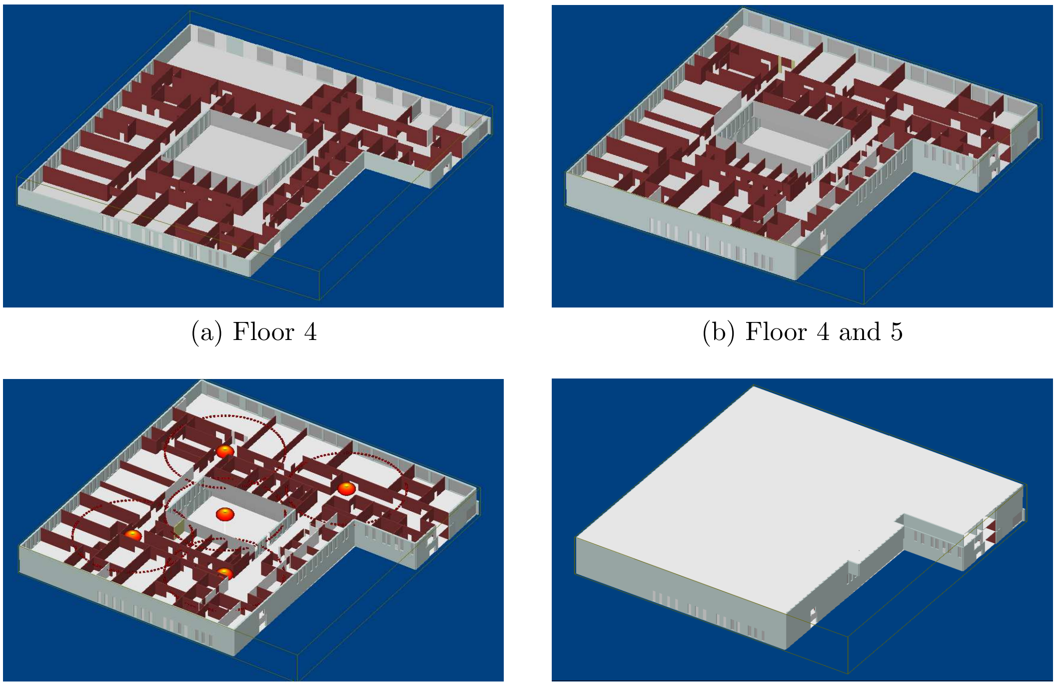

(a) Floor 4 (b) Floor 4 and 5

(c) Floor 4, 5, Tx and Rx (d) Total Study Area

Figure 3.7: Indoor wireless environment scenario.

of receivers was found to be sufficient to generate the required multipath signals within a reasonable simulation time. The distance between the transmitter and each receiver was D = 10 and 30 m for the indoor and outdoor scenarios, respectively. These distances are typical values used for the separation distance between the receiver and the transmitter in the indoor and picocellular outdoor wireless communication systems [2]. Therefore, for each location, the AOA of the received multipath signals were measured in both the azimuth and the elevation angles within a specified received power range. The transmitted power and the receiver's threshold was set to 0 dBW and −100 dBW, respectively. To minimize the effects of the structural geometries of the study area, the simulations were repeated at different transmitter locations. In the indoor simulation scenario, the fourth, fifth, and sixth floors of the Engineering and Information Technology Complex (EITC) at the University of Mani-

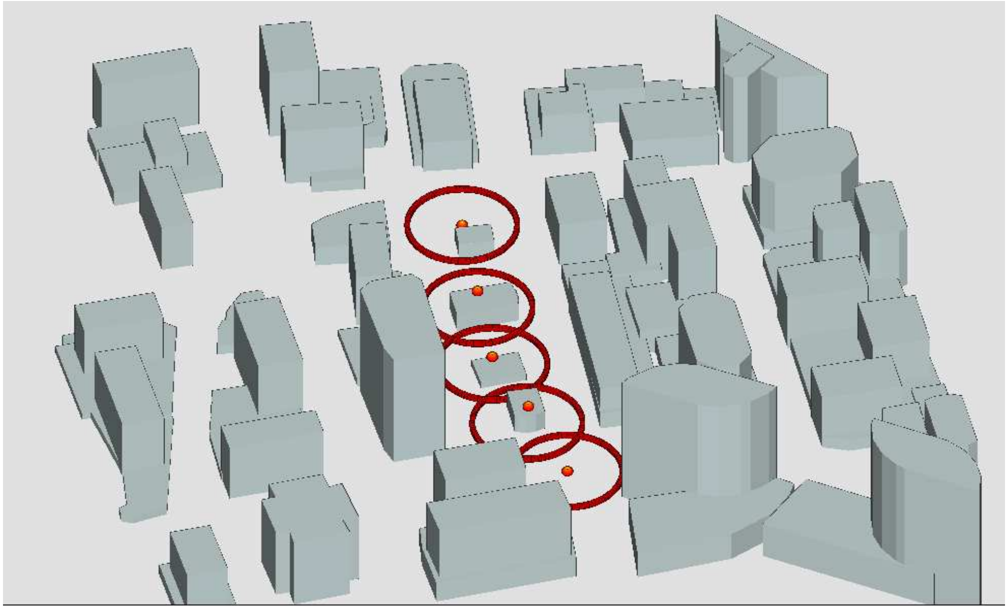

Figure 3.8: Outdoor wireless environment scenario

toba have been modeled to generate an indoor wireless communication environment. All the modeled building features, including its dimensions and material's electromagnetic properties have been defined. For example, brick and concrete for walls, and glass for windows have been imported from the software's library. The receivers, i.e. MS, were positioned within the fifth floor along a ring, while the transmitter, i.e. BS, was placed at the ring's center. An omnidirectional antenna was employed at both the transmitter's and the receiver's sides at an operation frequency of 2.4 GHz. To model an outdoor wireless environment, the Rosslyn city model which is available with the software, has been used, as shown in Figure 3.8. The simulation setting's parameters were the same as the indoor scenario setting's parameters except the distance between the transmitter and the receiver was set to $D = 30\ m$. The measured root mean square (RMS) angular spreads, i. e. standard deviation, in the azimuth and the elevation planes can be used for extracting the model's physical parameters, i.e. ellipsoid's eccentricities, to produce similar results. The theoretical rms angular spread can

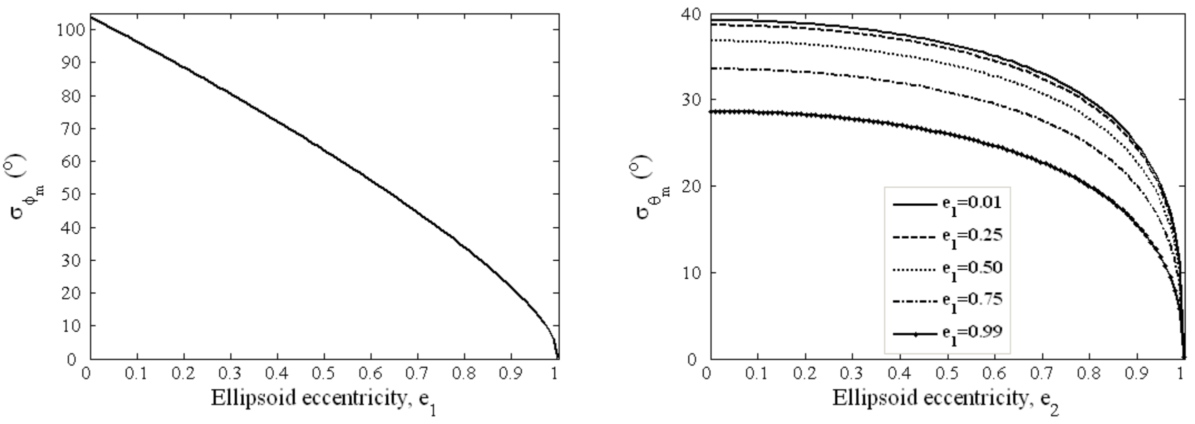

(a) σ_{ϕ_m} (b) σ_{θ_m}

Figure 3.9: a) RMS angular spread in the azimuth plane, σ_{ϕ_m}, versus ellipsoid eccentricity, e_1, b) RMS angular spread in the elevation plane, σ_{θ_m}, versus ellipsoid eccentricity,e_2, at different values of e_1.

be calculated as

$$\sigma_{\kappa_m} = \sqrt{E[\kappa_m^2] - E[\kappa_m]^2}, \tag{3.27}$$

where $E[\kappa_m]$ and $E[\kappa_m^2]$ are the mean, μ_{κ_m}, and the second moment of the random variable, κ, respectively. These quantities can be determined from their usual definitions as

$$E[\kappa_m] = \int \kappa_m f(\kappa_m) d\kappa_m, \tag{3.28}$$

$$E[\kappa_m^2] = \int \kappa_m^2 f(\kappa_m) d\kappa_m, \tag{3.29}$$

where κ_m can be used to represent the AOA random variables, ϕ_m and θ_m, while $f(\kappa_m)$ is the corresponding pdf. The means of the AOA in the azimuth and the elevation angles from the Wireless InSite simulated data were obtained as: $\mu_{\phi_m} = 180.48^o$, $\mu_{\phi_m} = 181.94^o$ and $\mu_{\theta_m} = 91.79^o$, $\mu_{\theta_m} = 88.86^o$ in indoor and outdoor simulation scenarios, respectively; where the theoretical mean values based on the proposed 3D model are: $\mu_{\phi_m} = 180^o$ measured from

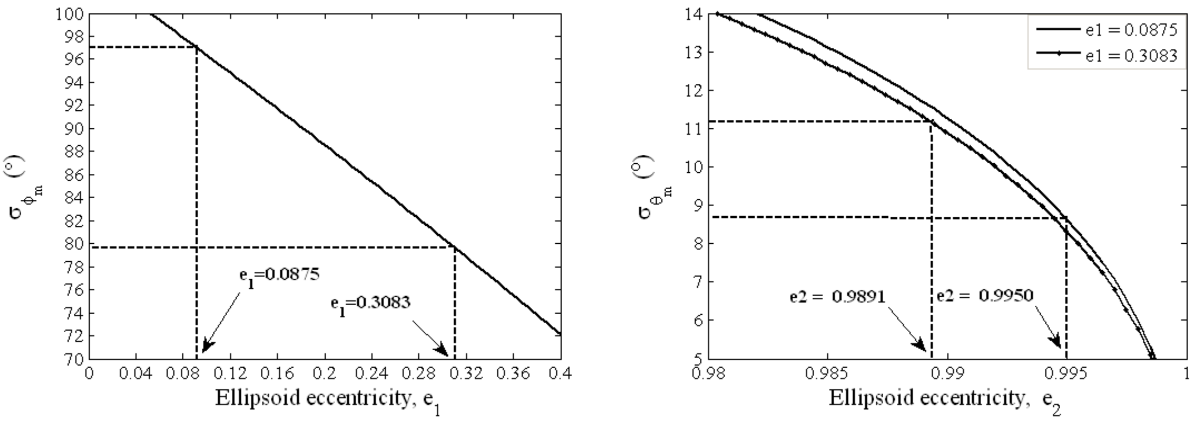

(a) σ_{ϕ_m} (b) σ_{θ_m}

Figure 3.10: a) RMS angular spread in the azimuth plane, σ_{ϕ_m}, versus ellipsoid eccentricity, e_1, within a specified range, b) RMS angular spread in the elevation plane, σ_{θ_m}, versus ellipsoid eccentricity, e_2, within a specified range, at two different values of e_1.

the x-axis and $\mu_{\theta_m} = 90^o$ measured from the z-axis.

The simulated angular spreads were obtained as: $\sigma_{\phi_m} = 79.82^o$, $\sigma_{\phi_m} = 97.32^o$ and $\sigma_{\theta_m} = 11.24^o$, $\sigma_{\theta_m} = 8.65^o$ at the indoor and outdoor examples, respectively. Therefore, values of $e_1 = 0.3086$ and $e_2 = 0.9891$ produced angular spreads of $\sigma_{\phi_m} = 79.82^o$ and $\sigma_{\theta_m} = 11.24^o$; whereas values of $e_1 = 0.0875$ and $e_2 = 0.9950$ produced angular spreads of $\sigma_{\phi_m} = 97.32^o$ and $\sigma_{\theta_m} = 8.65^o$. Then, for the given distances of $D = 10$ and $D = 30$ m and based on equations (3.9-3.11), the ellipsoid's semi-length can be determined. The measured AOA data has been used to create histograms containing 50 bins. The number of points in each bin was normalized to the total number of points to generate simulated pdfs. In order to measure the similarity between the theoretical and simulated pdfs' behavior, the cosine distance metric has been used. This metric has been widely used as a pattern similarity measure [60, 61].

The cosine distance $sim(p,q)$ is defined as:

$$sim(p,q) = \frac{\sum_{i=1}^{m} p_i q_i}{\sqrt{\sum_{i=1}^{m} p_i^2}\sqrt{\sum_{i=1}^{m} q_i^2}} \tag{3.30}$$

where m is the number of bins, i.e. number of interval, and q and p are corresponding the output of the two pdfs that need to be compared. Note that $sim(p,q)$ ranges in $[0,1]$, with $sim(p,q) = 1$ indicating that the two pdfs are identical. Therefore, the marginal pdfs in the azimuth and the elevation angles have been integrated on 50 interval, in order to convert the continuous pdfs to discrete probability mass functions (pmfs). Figure 3.11a and Figure 3.11b show the comparisons of theoretical and simulated pmfs in the azimuth and the elevation angles, respectively, for the indoor scenario, while the comparisons of the outdoor scenario are shown in Figure 3.12a and Figure 3.12b. As illustrated, comparison results show good agreement between the proposed and the simulated pmfs in both the azimuth and the elevation angles. The cosine distance metric shown that the similarity between the theoretical and simulated pmfs are: 0.9951 i.e. Figure 3.11a, and 0.9300 i.e. Figure 3.11b, in the azimuth and elevation angle, respectively, at indoor example, while for outdoor example the results are 0.9979, i.e. Figure 3.12a, and 0.8811 i.e. Figure 3.11b, in the azimuth and the elevation angles, respectively. The results illustrate one of the advantages of the geometric scattering channel model in comparison to site-specific propagation prediction software. The Wireless InSite software spends 3.90 and 1.25 hours to complete simulations of the indoor and the outdoor scenarios, respectively. The same results can be obtained within a few seconds by using a matlab code based on the proposed 3D geometrical scattering channel model. The simulations have been done using a dual core processor computer at 3.00 GHz

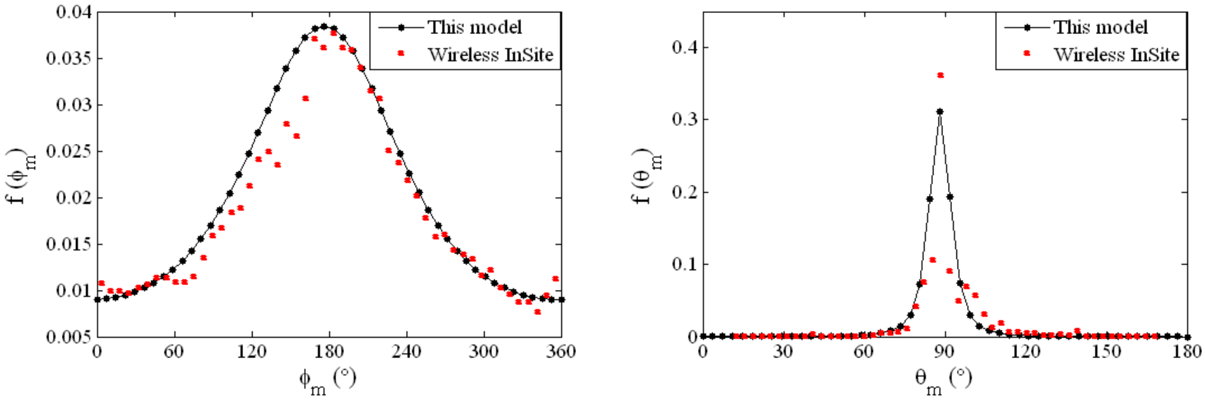

(a) $f(\phi_m)$ (b) $f(\theta_m)$

Figure 3.11: Comparison of the theoretical and simulated pmfs of the AOA for the indoor scenario: a) In the azimuth angle, and b) In the elevation angle.

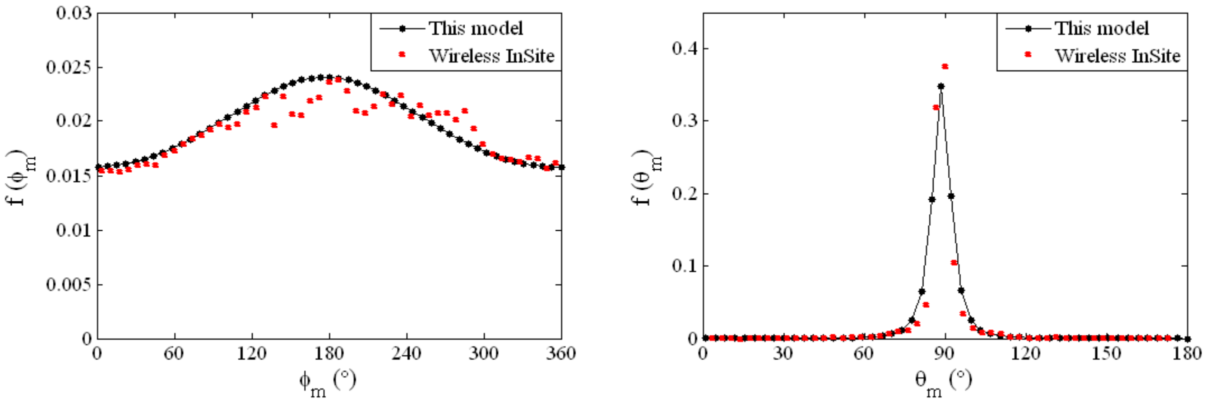

(a) $f(\phi_m)$ (b) $f(\theta_m)$

Figure 3.12: Comparison of the theoretical and simulated pmfs of the AOA for the outdoor scenario: a) In the azimuth angle, and b) In the elevation angle.

and 4 GB of RAM.

Chapter 4

Angle and Time of Arrival Statistics for a Three Dimensional Geometrical Scattering Channel Model

4.1 Introduction

In this chapter, a 3D geometrical scattering channel model for wireless propagation environments is introduced. This model is based on the assumption that the scatterers are distributed within a spheroid, in which the BS and MS are located at the spheroid's foci, i.e. 3D spheroidal model. The model captures both the spatial and temporal statistical distributions of the received multipath signals. Several angle of arrival and time of arrival probability density functions of the received multipath signals are provided in compact forms. Numerical results are presented to illustrate and verify the derived expressions. To validate the model, it has been compared against some available two dimensional models and measured data.

4.2 Model's Description

The model's description is similar to the ellipsoid model' description that described in Section 3.2. The spheroid's volume can be limited by the maximum observation time, τ_{max}, and each

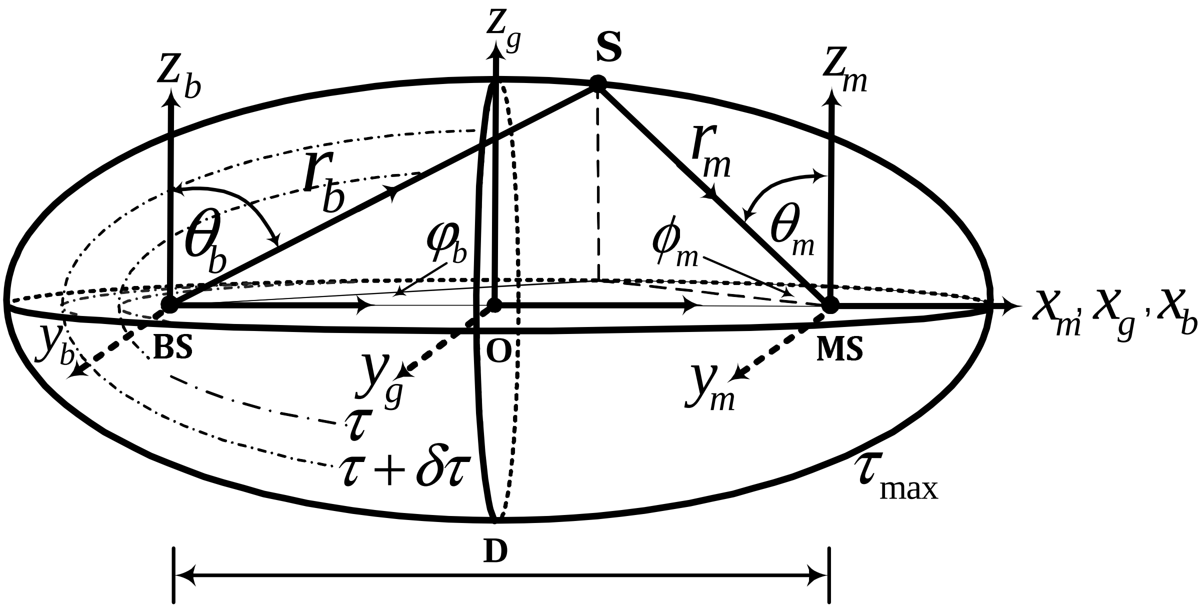

Figure 4.1: Spheroid model's geometry.

spheroid layer is corresponding to a certain value of the TOA of the multipath signals as shown in Figure 4.1. This spheroid model is consider as special from the previously developed ellipsoid model, in which the spheroid's semi-lengths on the minor axes, i.e. y-axis and z-axis, are assumed to be equal. Therefore, by substituting $b = c$ into (3.7), result in the radial distance, r_m, that can be used to describe the spheroid as seen from it's focal point, i.e the MS location.

$$r_m = \frac{2b^2}{(2a + D \sin\theta_m \cos\phi_m)}. \tag{4.1}$$

Similarly, due to the symmetry in the model's geometry, the radial distance as seen from the BS side, r_b, can be obtained as

$$r_b = \frac{2b^2}{(2a - D \sin\theta_b \cos\phi_b)}. \tag{4.2}$$

The total communication path length that results from a scatterer located on the spheroid's surface is given by

$$r_b + r_m = 2a = c\tau_{max}, \tag{4.3}$$

where c is the speed of light and τ_{max} is the maximum observation time. Thus, the model's parameters a and b may be expressed as

$$a = \frac{c\,\tau_{max}}{2}, \tag{4.4}$$

$$b = \frac{\sqrt{c^2\tau_{max}^2 - D^2}}{2}. \tag{4.5}$$

The spheroid's semi-lengths can be related as $b = a\sqrt{1-e^2}$ and the spheroid's eccentricity is defined as $e = D/2a$. Therefore, the radial distances, r_m and r_b, can be obtained as

$$r_m = \frac{c^2\tau_{max}^2 - D^2}{2(c\tau_{max} + D\sin\theta_m\cos\phi_m)}, \tag{4.6}$$

$$r_b = \frac{c^2\tau_{max}^2 - D^2}{2(c\tau_{max} - D\sin\theta_b\cos\phi_b)}, \tag{4.7}$$

where (θ_m, ϕ_m) and (θ_b, ϕ_b) are the AOA of the received multipath signals in the elevation and azimuth planes as seen from the MS and BS respectively. The AOA as seen from the BS can be considered as the angle of departure (AOD) of the transmitted signals.

4.3 Angle and Time of Arrival Probability Density Functions

The objective of this chapter is to determine the AOA and TOA pdfs of the multipath signals, where the scatterers are assumed to be distributed uniformly within the spheroid's volume and the BS and MS are located at the spheroid's foci.

4.3.1 Angle of Arrival Joint Probability Density Function

The AOA joint pdf $f(\theta_m, \phi_m)$ of the received multipath signals can be obtained by determining the probability of the i^{th} signal that arrives at the MS antenna within a certain range of the AOA, (θ_m, ϕ_m), such that $0 < \theta_m^i \leq \theta_m$ and $0 < \phi_m^i \leq \phi_m$. As shown in Figure 4.1, all scatterers inside the spheroid cause multipath signals to arrive at the MS antenna at a TOA, τ, such that $\tau_o < \tau \leq \tau_{max}$, where τ_o and τ_{max} are the TOA of the LOS component and the maximum observation time, respectively. Typically, τ_{max} is determined according to available criteria based on desired channel characteristics [3]. The probability is obtained by normalizing the spheroid's slice, $V_{\tau_{max}}(\theta_m, \phi_m)$, to the total volume of the spheroid, $V_{\tau_{max}}$. These quantities are defined by

$$\begin{aligned} V_{\tau_{max}}(\theta_m, \phi_m) &= \int_0^{r_m} \int_0^{\phi_m} \int_0^{\theta_m} r^2 \sin\alpha_m dr d\alpha_m d\beta_m \\ &= \int_0^{\phi_m} \int_0^{\theta_m} \frac{(c^2\tau_{max}^2 - D^2)^3 \sin\alpha_m}{24(c\tau_{max}^2 + D\sin\alpha_m \cos\beta_m)^3} d\alpha_m d\beta_m, \end{aligned} \tag{4.8}$$

and

$$V_{\tau_{max}} = \frac{\pi c\tau_{max}(c^2{\tau_{max}}^2 - D^2)}{6}, \tag{4.9}$$

Therefore, the probability of multipath components arriving at the MS within the specified range is given by

$$
\begin{aligned}
p_r(0 < \theta_m^i \leq \theta_m, 0 < \phi_m^i \leq \phi_m) &= F(\theta_m, \phi_m) \\
= \int_0^{\phi_m} \int_0^{\theta_m} & \frac{(c^2\tau_{max}^2 - D^2)^2 \sin\alpha_m}{4\pi c\tau_{max}(c\tau_{max} + D\sin\alpha_m \cos\beta_m)^3} \\
& d\alpha_m d\beta_m,
\end{aligned}
\tag{4.10}
$$

where $F(\theta_m, \phi_m)$ is the AOA joint cumulative distribution function (CDF). Therefore the AOA joint pdf may be obtained by taking the partial derivative of (4.10) with respect to θ_m and ϕ_m. This gives

$$
\begin{aligned}
f(\theta_m, \phi_m) &= \frac{(c^2\tau_{max}^2 - D^2)^2 \sin\theta_m}{4\pi c\tau_{max}(c\tau_{max} + D\sin\theta_m \cos\phi_m)^3}, \\
& 0 < \theta_m \leq \pi \ , \quad 0 < \phi_m \leq 2\pi.
\end{aligned}
\tag{4.11}
$$

Similarly, due to the symmetry in the model's geometry, the AOA joint pdf at the BS can be obtained by using (4.7). This gives

$$
\begin{aligned}
f(\theta_b, \phi_b) &= \frac{(c^2\tau_{max}^2 - D^2)^2 \sin\theta_b}{4\pi c\tau_{max}(c\tau_{max} - D\sin\theta_b \cos\phi_b)^3}, \\
& 0 < \theta_b \leq \pi \ , \quad 0 < \phi_b \leq 2\pi.
\end{aligned}
\tag{4.12}
$$

4.3.2 Angle of Arrival Joint Probability Density Function Conditioned on the Time of Arrival

The AOA pdf conditioned on the TOA of the multipath signals, $f(\theta_m, \phi_m|\tau)$, is determined based on the assumption that the scatterers are uniformly distributed within a 3D space that is limited by two spheroids corresponding to τ and $\tau + \delta\tau$ as shown in Figure 4.1. The normalization of the difference in volumes of the two spheroids' slices to the relative difference in their total volumes provides the probability for the multipath signals' arrival within specified AOA and TOA intervals, shown as

$$\begin{aligned} p(0 < \theta_m^i \leq \theta_m \,,\, 0 < \phi_m^i \leq \phi | \tau < \tau_i \leq \tau + \delta\tau) &= F(\theta_m, \phi_m | \tau) \\ &= \frac{V_{\tau+\delta\tau}(\theta_m, \phi_m) - V_\tau(\theta_m, \phi_m)}{V_{\tau+\delta\tau} - V_\tau}, \end{aligned} \tag{4.13}$$

where

$$\begin{aligned} &V_\tau(\theta_m, \phi_m) = \\ &\quad \int_0^{\phi_m} \int_0^{\theta_m} \frac{(c^2\tau^2 - D^2)^3 \sin\alpha_m}{24(c\tau + D\sin\alpha_m \cos\beta_m)^3} d\alpha_m d\alpha_m, \end{aligned} \tag{4.14}$$

$$\begin{aligned} &V_{\tau+\delta\tau}(\theta_m, \phi_m) = \\ &\quad \int_0^{\phi_m} \int_0^{\theta_m} \frac{(c^2(\tau+\delta\tau)^2 - D^2)^3 \sin\alpha_m}{24(c(\tau+\delta\tau) + D\sin\alpha_m \cos\beta_m)^3} d\alpha_m d\beta_m, \end{aligned} \tag{4.15}$$

$$V_\tau = \frac{\pi\, c\tau\, (c^2\tau^2 - D^2)}{6}, \tag{4.16}$$

$$V_{\tau+\delta\tau} = \frac{\pi c(\tau+\delta\tau)(c^2(\tau+\delta\tau)^2 - D^2)}{6}. \tag{4.17}$$

Substituting (4.14)-(4.17) into (4.13), dividing both the numerator and denominator by $\delta\tau$ and taking the limit when $\delta\tau$ goes to zero [3], results in

$$p(0 < \theta_m^i \leq \theta_m, 0 < \phi_m^i \leq \phi | \tau < \tau_i \leq \tau + \delta\tau) = \lim_{\delta\tau \to 0} \left(\frac{\left(\frac{V_{\tau+\delta\tau}(\theta_m,\phi_m) - V_\tau(\theta_m,\phi_m)}{\delta\tau} \right)}{\left(\frac{V_{\tau+\delta\tau} - V_\tau}{\delta\tau} \right)} \right) = \frac{\acute{V}_\tau(\theta_m, \phi_m)}{\acute{V}_\tau}, \tag{4.18}$$

where $\acute{V}_\tau(\theta_m, \phi_m)$ and $\acute{V}_\tau$ are the derivations of (4.14) and (4.16) with respect to τ. Substituting the derivations of (4.14) and (4.16) into (4.18) and simplifying, results in

$$\begin{aligned} p(0 < \theta_m^i \leq \theta_m\, , \, 0 < \phi_m^i \leq \phi_m | \tau < \tau_i \leq \tau + \delta\tau) &= F(\theta_m, \phi_m | \tau) \\ &= \int_0^{\phi_m} \int_0^{\theta_m} f(\alpha_m, \beta_m | \tau) d\alpha_m d\beta_m, \end{aligned} \tag{4.19}$$

where $f(\theta_m, \phi_m|\tau)$ is the AOA joint pdf conditioned on the TOA which is given by

$$f(\theta_m, \phi_m|\tau) = \frac{3(c^2\tau^2 - D^2)^2(c^2\tau^2 + 2\, c\tau\, D \sin\theta_m \cos\phi_m + D^2) \sin\theta_m}{4\pi\, (3\, c^2\tau^2 - D^2)(c\tau + D \sin\theta_m \cos\phi_m)^4}. \tag{4.20}$$

Similarly, the AOA joint pdf conditioned on the TOA as seen from the BS is given as

$$f(\theta_b, \phi_b|\tau) = \frac{3(c^2\tau^2 - D^2)^2(c^2\tau^2 - 2\, c\tau\, D \sin\theta_b \cos\phi_b + D^2) \sin\theta_b}{4\pi\, (3\, c^2\tau^2 - D^2)(c\tau - D \sin\theta_b \cos\phi_b)^4}. \tag{4.21}$$

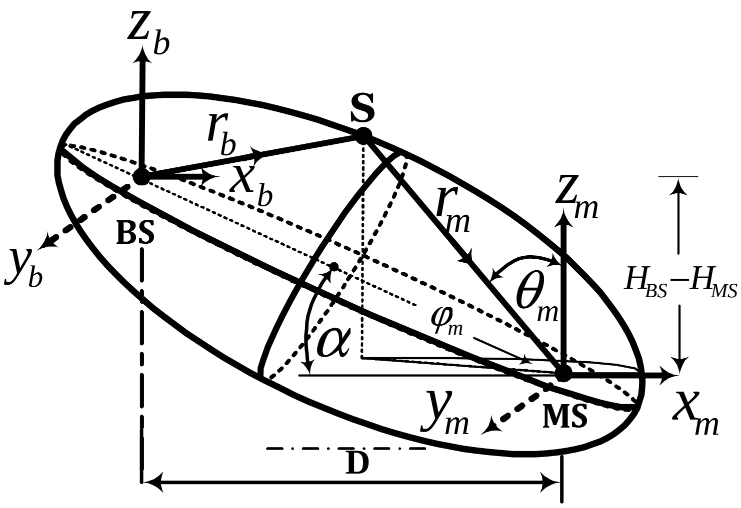

Figure 4.2: Elevated BS model's geometry.

4.3.3 Angle and Time of Arrival Probability Density Functions for an Elevated Base Station

In some outdoor and indoor wireless communication scenarios, the BS antennas are elevated in comparison to the MS antennas. To include the antennas relative difference in heights of the BS and MS antennas, the spheroid model's geometry can be inclined as shown in Figure 4.2, where α is the inclination angle, which is given by

$$\alpha = \tan^{-1}\left(\frac{H_{BS} - H_{MS}}{D}\right), \tag{4.22}$$

where H_{BS} and H_{MS} are the heights of the BS and MS antennas, respectively. In such a case, the radial distance r_m can be derived as

$$r_m = \frac{c^2\tau_{max}^2 - D^2}{2(c\tau_{max} + D(\sin\theta_m \cos\phi_m \cos\alpha - \sin\theta_m \sin\alpha)}. \tag{4.23}$$

Therefore, all derived AOA pdfs can be modified to include the difference in heights between the BS and MS. For example, the AOA joint pdf at the MS may be given by

$$f(\theta_m, \phi_m) = \frac{(c^2\tau_{max}^2 - D^2)^2 \sin\theta_m}{4\pi c\tau_{max}(c\tau_{max} + D(\sin\theta_m \cos\phi_m \cos\alpha - \sin\theta_m \sin\alpha))^3}. \tag{4.24}$$

4.3.4 Time of Arrival Marginal Probability Density Function

The probability that the multipath components arrive with a delay, τ, such that $\tau_o < \tau \leq \tau_{max}$ can be obtained by normalizing the V_τ to $V_{\tau_{max}}$. These quantities, i.e. V_τ and $V_{\tau_{max}}$, are given in (4.16) and (4.9). Therefore, normalizing (4.18) to (4.9), results in

$$\begin{aligned} p_r(\tau_o < \tau \leq \tau_{max}) &= F(\tau) \\ &= \frac{\tau\left(c^2\tau^2 - D^2\right)}{\tau_{max}\left(c^2{\tau_{max}}^2 - D^2\right)}, \end{aligned} \tag{4.25}$$

where $F(\tau)$ is the TOA marginal CDF. Differentiating (4.25) with respect to τ results in the TOA marginal pdf

$$f(\tau) = \frac{3\,c^2\tau^2 - D^2}{\tau_{max}\left(c^2{\tau_{max}}^2 - D^2\right)}, \qquad \tau_o < \tau \leq \tau_{max}. \tag{4.26}$$

4.4 Numerical Results and Model's Validations

To illustrate and verify the developed 3D model, several numerical 2D and 3D results are provided for the AOA and TOA pdfs. Figure 4.3a and Figure 4.3b show the 3D graph of the AOA joint pdfs at the MS $f(\theta_m, \phi_m)$ and BS $f(\theta_b, \phi_b)$ respectively, for $\tau = 1.5\tau_o$, where τ_o is

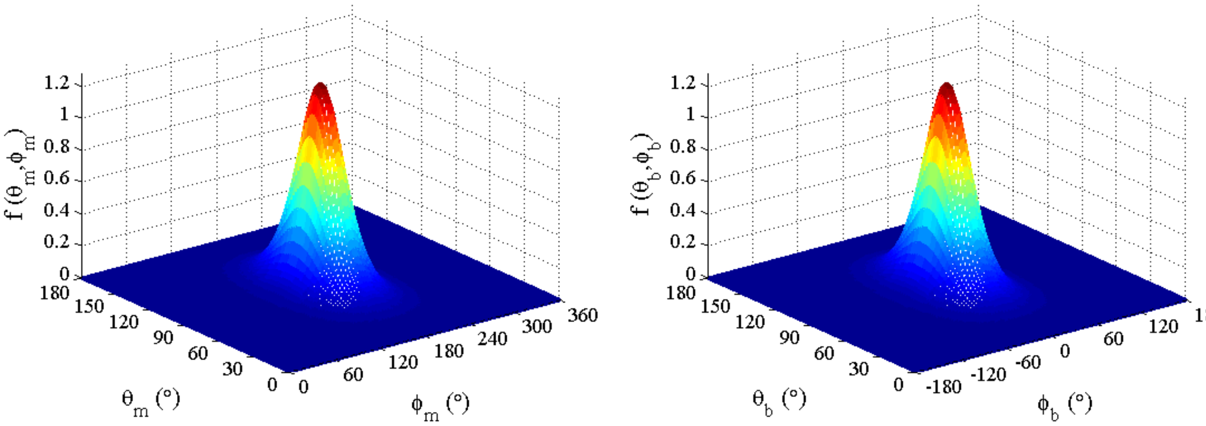

(a) $f(\theta_m, \phi_m)$ (b) $f(\theta_b, \phi_b)$

Figure 4.3: The AOA joint pdfs at the MS and BS for $\tau_{max} = 1.5\tau_o$

the TOA of the LOS component. It is clear that the most frequent occurrences of the AOA take place around the relative direction between the MS and BS in both the elevation angle, $\theta_m = 90^o$, and azimuth angle, $\phi_m = 180^o$ and $\phi_b = 0^o$.

To verify the AOA and TOA expressions, they have been compared with histogram simulated pdfs. The histograms were created by simulating $200,000$ scatterers uniformly distributed within the spheroid's volume, where the spheroid's semi-lengths were the same as those used in plotting the theoretical pdfs. As such, for all scatterers the desired AOA and TOA of the multipath signals were calculated based on the location of the scatterers, the MS and the BS. A histogram containing 50 bins (intervals) was then created and the number of points in each bin was normalized to the total number of points.

Figure 4.4a and Figure 4.4b show the plots of the theoretical and simulated AOA pdfs in the azimuth angle, $f(\phi_m)$, and BS, $f(\phi_b)$, respectively, and the plot of the AOA pdf in the elevation angle, $f(\theta_m)$, is shown in Fig.4.4c. The pdfs have been illustrated for various values of maximum observation time, $\tau_{max} = 1.5\tau_o, 2.0\tau_o$, and $3.0\tau_o$. These figures illustrate that the

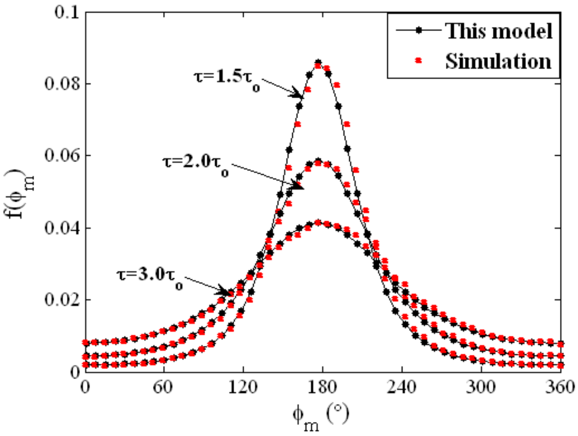

(a) $f(\phi_m)$

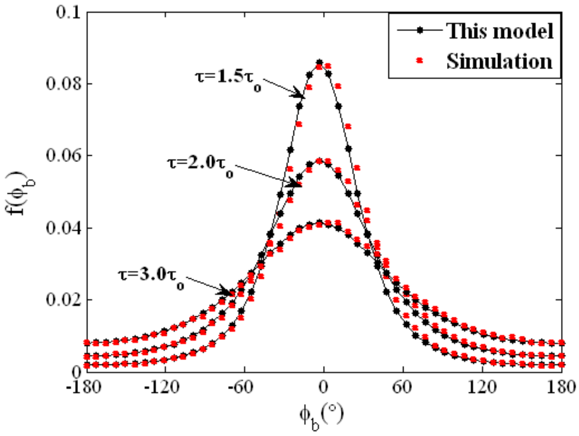

(b) $f(\phi_b)$

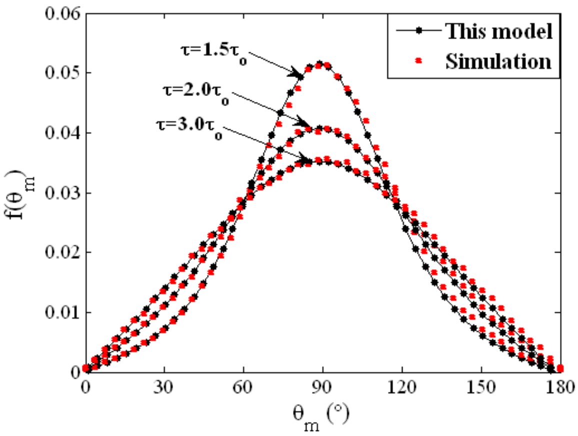

(c) $f(\theta_m)$

Figure 4.4: The AOA marginal pdfs in the azimuth and elevation angle as seen from the MS and BS for $\tau_{max} = 1.5, 2.0$, and $3.0\tau_o$.

angular spread in the elevation and azimuth planes increases with an increasing maximum observation time. In other words, the azimuth and elevation angular spread depends on the maximum observation time at fixed separation distances. Consistent agreement between the theoretical and simulated graphs is clearly illustrated in all the AOA pdfs.

Figure 4.5a and Figure 4.5b illustrate the 3D plots of the AOA and TOA joint pdfs in the azimuth angle, $f(\tau, \phi_m)$, and elevation angle, $f(\tau, \theta_m)$, respectively, for $\tau_{max} = 5\tau_o$. It is clear that by increasing the maximum observation time, τ_{max}, the AOA distribution in the azimuth

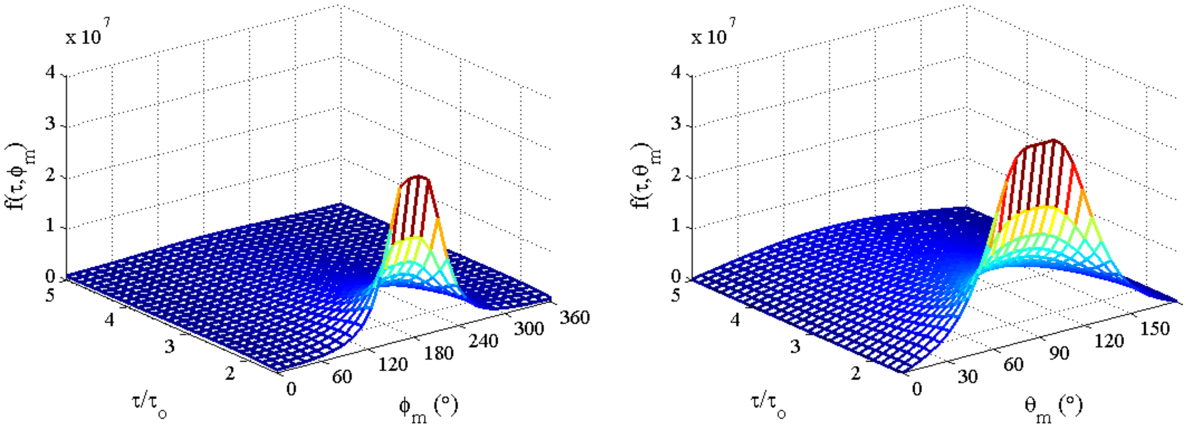

(a) $f(\tau, \phi_m)$ (b) $f(\tau, \theta_m)$

Figure 4.5: The AOA and TOA joint pdfs at the MS for $\tau_{max} = 5\tau_o$.

angle approaches a uniform distribution, $f(\phi_m) = 1/2\pi$, and the AOA distribution in the elevation angle approaches a sinusoidal distribution, $f(\theta_m) = \sin(\theta_m)$. These results agree with the azimuthal and elevational angular distributions when the scatterers are assumed to be uniformly distributed within a sphere, since the spheroid geometry can approximate a sphere for large values of τ_{max}.

Figure 4.6 shows the AOA pdfs for different inclination angles, $\alpha = 0^o$, 10^o and 20^o, for a separation distance of $D = 30$ m, which results in 0, 5.3, and 11 m of difference between the BS and MS antennas, respectively. Clearly, the most of AOA are around $\theta_m = 90^o$, 80^o, and 70^o, for $\alpha = 0^o$, 10^o and 20^o respectively. Figure 4.7 shows the plot of the marginal TOA pdf as a function of the normalized TOA, τ/τ_o, for $\tau_{max} = 3.0\tau_o$. As illustrated, the graph increases with an increase in the TOA.

To validate the developed geometrical scattering channel model, the model has been compared against similar 2D models. For example, the AOA marginal and conditioned pdfs as seen from the MS have been proposed based on the 2D elliptical model [16], i.e. $\theta_m = 90^o$,

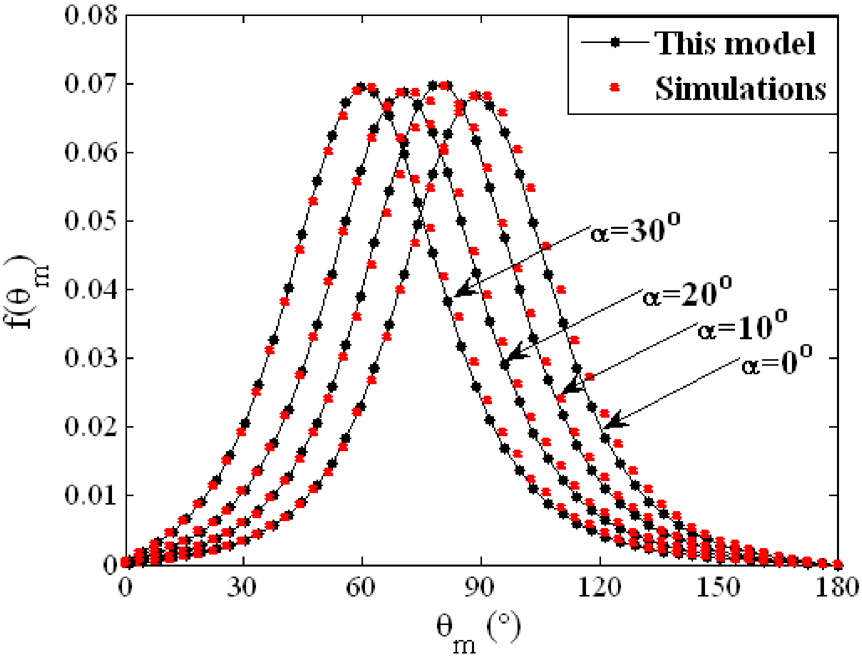

Figure 4.6: The AOA pdf $f(\theta_m)$ for $\alpha = 0^o$, 10^o and 20^o.

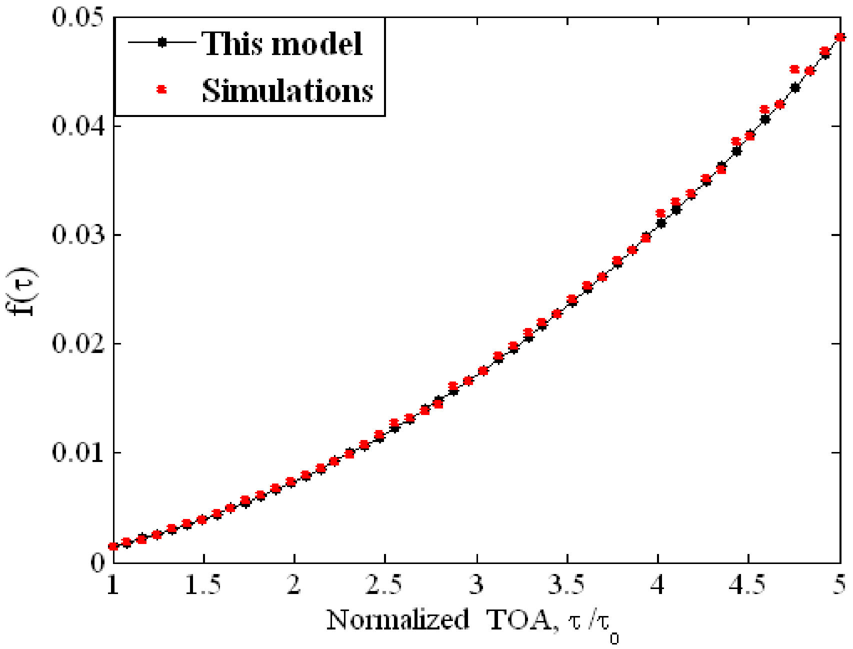

Figure 4.7: The TOA pdf, $f(\tau)$, in terms of the normalized TOA, τ/τ_o.

where the elliptical model is generalized in, [22], to obtain the marginal pdfs as seen from both the MS and BS. The developed 3D spheroidal model can be reduced to obtain the AOA pdfs in the azimuth plane that have been derived based on the 2D models, as shown by

$$f(\phi_m)_{2D} = \left. \frac{f(\theta_m, \phi_m)_{3D}}{\int_0^{2\pi} f(\theta_m, \phi_m)_{3D} d\phi_m} \right|_{\theta_m = 90^\circ}, \tag{4.27}$$

$$f(\phi_m/\tau)_{2D} = \left. \frac{f(\theta_m, \phi_m|\tau)_{3D}}{\int_0^{2\pi} f(\theta_m, \phi_m|\tau)_{3D} d\phi_m} \right|_{\theta_m = 90^\circ}. \tag{4.28}$$

Figure 4.8a Figure 4.8c illustrate the comparisons of the AOA marginal and conditioned pdfs that have been determined based on the proposed 3D spheroids model and Liberti's 2D model [16]. Similarly, the AOA marginal pdf as seen from the BS compared with Ertel's 2D model [22] is illustrated in Figure 4.8b. All plots illustrate exact agreement between the proposed 3D model and the similar 2D models. Furthermore, the model has been compared against the validated 2D geometrical scattering channel models [24,33,36]. These 2D models have been validated by comparing their AOA pdfs in the azimuth angle with some of the available measured data [62–64]. The derived AOA joint pdf as seen from the BS can be obtained by

$$f(\phi_b)_{2D} = \left. \frac{f(\theta_b, \phi_b)_{3D}}{\int_0^{2\pi} f(\theta_b, \phi_b)_{3D} d\phi_b} \right|_{\theta_b = 90^\circ}, \tag{4.29}$$

where $f(\theta_b, \phi_b)$ is the AOA joint pdf as seen from the BS, which is given by

$$f(\theta_b, \phi_b) = \frac{(1 - e^2)^2 \sin\theta_b}{4\pi(1 - e \sin\theta_b \cos\phi_b)^3}. \tag{4.30}$$

The measured RMS angular spreads can be used in extracting the model's physical param-

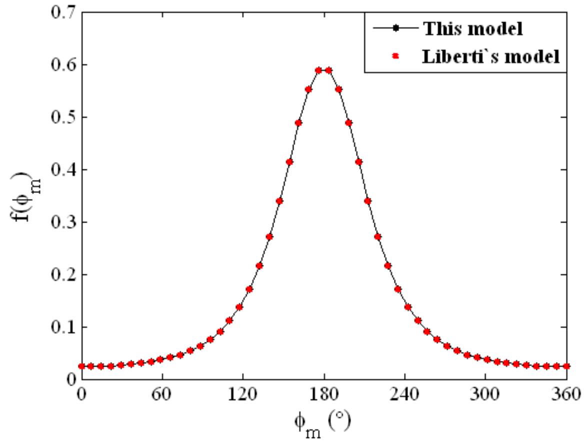

(a) $f(\phi_m)$

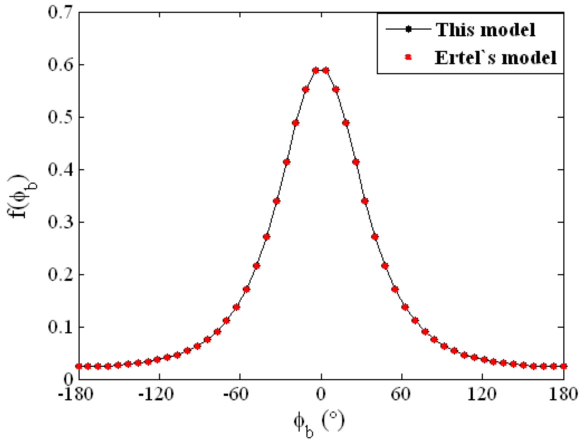

(b) $f(\phi_b)$

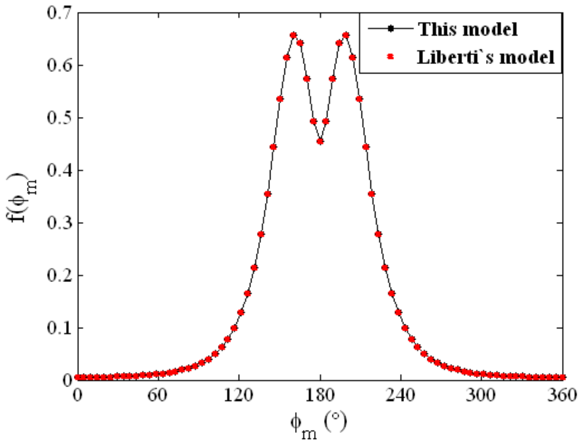

(c) $f(\theta_m)$

Figure 4.8: Comparison of AOA pdf in the azimuth angle with Liberti's [16] and Ertel's [22] 2D models.

eters, i.e. spheroid's eccentricity, to produce similar results. The theoretical RMS angular spread can be obtained based on equations (3.27-3.29). The plot of the RMS angular spread in the azimuth angle, σ_{ϕ_b}, versus the spheroid's eccentricity, e, is shown in Figure 4.9. Pedersen *et al.*, in [62], conducted outdoor channel measurements in the urban areas of Aarhus, Denmark and Stockholm, Sweden. Wideband measurements were conducted at a carrier frequency of 1.8 GHz and at a sampling time of 122 ns. The measured angular data

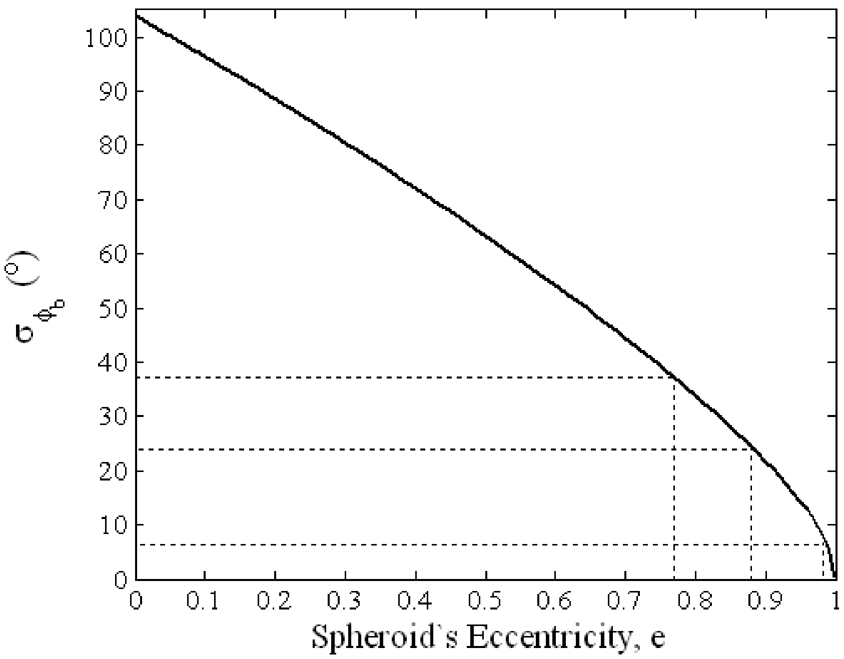

Figure 4.9: RMS angular spread, σ_{ϕ_b}, versus spheroid eccentricity, e.

had a standard deviation of 6^o. Spencer *et al.*, in [63], conducted indoor channel measurements within office buildings in the Brigham Young University (BYU) campus. The data was collected at 7 GHz in the angle and time domains, with impulse response measurements carried out using a narrow-beam dish antenna. The AOA measurements had a standard deviation in angle of 24.5^o. Cramer *et al.*, in [64], collected data in an office/laboratory building. In the experiment, the location of the transmit antenna was fixed, and rectangular arrays of measurements were made by moving the receive antenna to 49 points in a 7×7 array. They showed that the relative azimuth AOA of the recovered ultra-wideband signals gave the best fit for a Laplacian distribution, with a standard deviation of 38^o. Accordingly, as shown in Figure 4.9, values of $e = 0.99$, 0.88 and 0.76 are required to produce standard deviation of 6^o, 24.4^o and 38^o respectively, where $e = D/2a$. In literature, three 2D geometrical channel models [24,33,36] have been validated by comparing their pdfs of the AOA

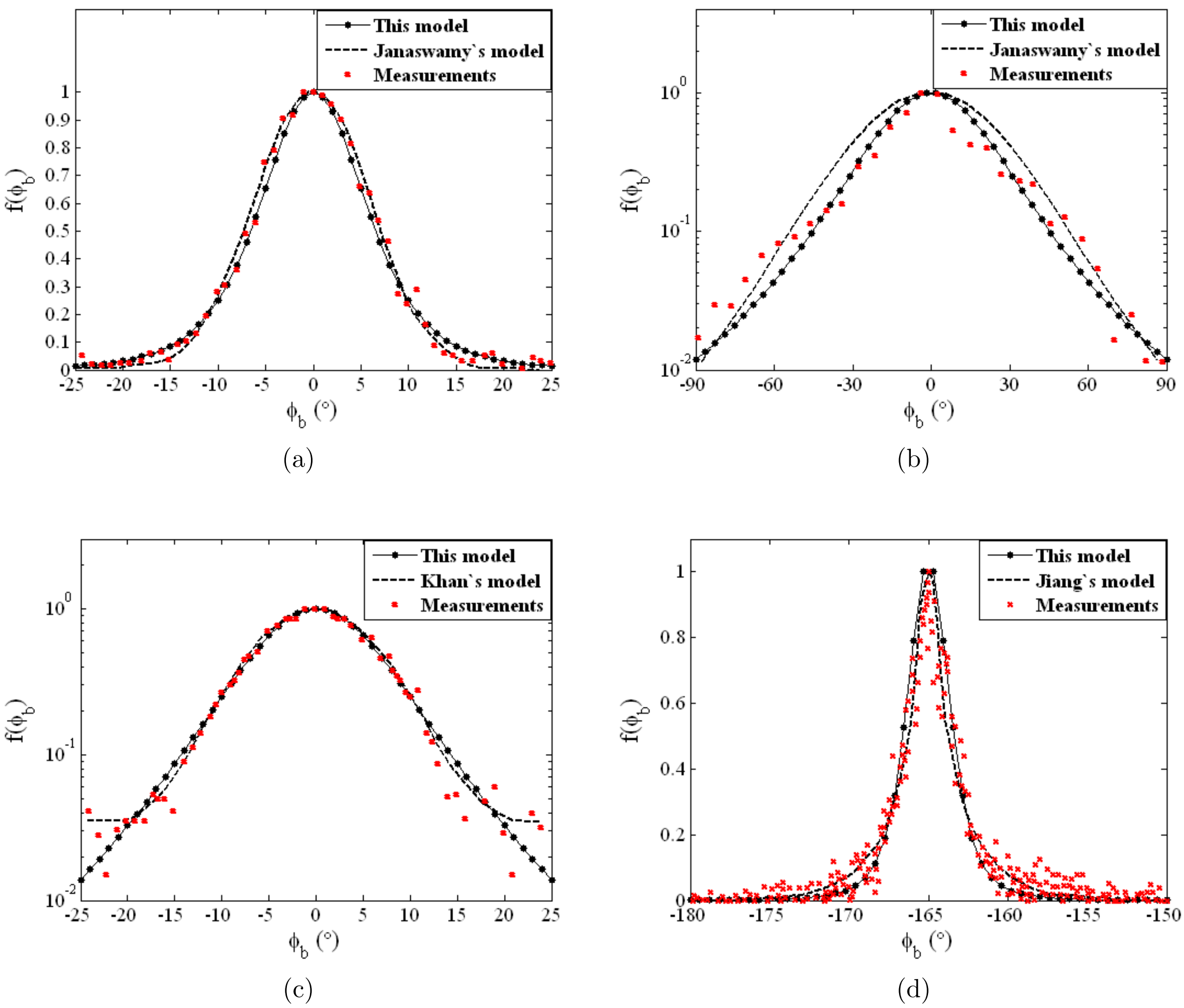

Figure 4.10: Comparison of AOA expressions in the azimuth angle with: a) Janaswamy's 2D model [24] and measurements [62], b) Janaswamy's model [4] and measurements [63], c) Khan's model [36] and measurements [62] and d) Jiang's model [33] and measurements [64].

with these measured data. Therefore, in order to validate, the developed 3D models, the pdf of AOA in the azimuth angle have been compared with both the 2D models and the channel measured data. Since the channel measured data are unavailable, therefore, both the 2D pdfs and the measured data have been digitized from their corresponding references [24, 33, 36]. Also, to make comparisons easier, the plots for the AOA pdfs, have been normalized for their maximum values. As shown in Fig 4.10, the comparisons of the derived AOA pdfs in the azimuth angle with the 2D geometrical scatterering channel models and the corresponding measured channel data are provided. As illustrated, comparison' results show good agreement between the proposed 3D model and the 2D models, as well as, the measured data. A log scale has been used in Figure 4.10b and Figure 4.10c to permit easier comparisons as provided in [24, 36].

Chapter 5

Angle and Time of Arrival Statistics for a Three Dimensional Gaussian Scatterers Density Model

5.1 Introduction

In Chapter 4, the ellipsoidal geometrical scattering channel model has been extended to include the TOA of the received multipath fading signals, where the scatterers are assumed to be uniformly distributed within the spheroid's volume. However, it has been observed that the scatterers density decreases with increasing distance from the MS antenna, because the scatterers in close proximity to the MS antenna make a greater contribution to signal scattering than remote scatterers. Therefore, the 2D Gaussian scatterers density model has been suggested in the literature [24, 36, 41, 65–67] to obtain the AOA and TOA pdfs of the multipath signals. From a physical viewpoint, it seems reasonable to assume that the scatterers density gradually taper off with distance from the BS antennas in both the azimuth and elevation angles. This assumption lead to more accurate predictions in some of the wireless communication scenarios. Therefore, in this chapter, an extension of the 3D spheroidal model with a general distribution of scatterers is introduced. For this special case,

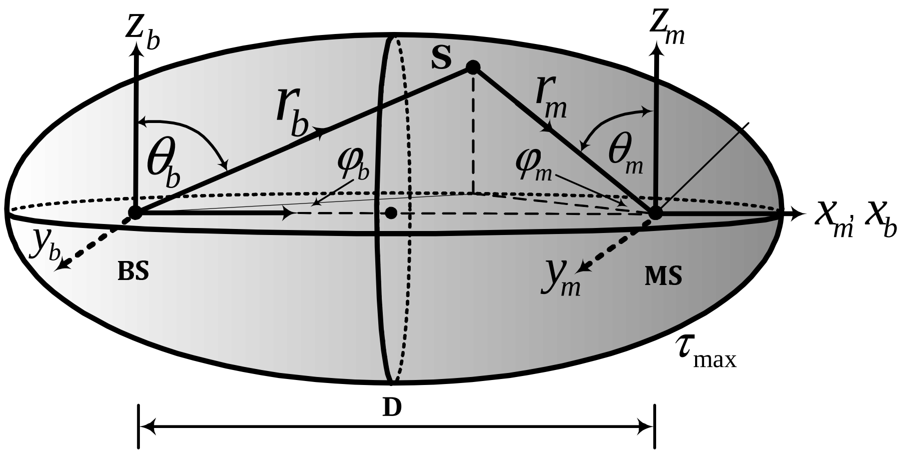

Figure 5.1: 3D Gaussian model's geometry

the 3D Gaussian scatterers density model has been considered. Expressions for the AOA and TOA joint pdfs of the multipath fading signals have been obtained as seen from both the MS and BS.

5.2 Model's Description.

The 3D model's geometry is shown in Figure 5.1. The model's description is similar to the ellipsoid and spheroid model's description that has been given in Sections 3.2 and 4.2, respectively. However, the scatterers density around the MS is assumed to follow a general scatterers distribution.

5.3 Angle and Time of Arrival Joint Probability Density Functions

The objective is to determine the joint pdfs of the AOA and TOA of the received multipath signals, as seen from the MS and the BS, for a given scatterers density function, $f(x_m, y_m, z_m)$, at the MS, i.e. the MS is assumed to be located at the center of the scatterers and the scatterers density may include the BS. The joint pdf of the AOA and TOA, $f(\tau, \theta_m, \phi_m)$, can be obtained by making use of the Jacobian transformation. This gives

$$f(r_m, \theta_m, \phi_m) = \left. \frac{f(x_m, y_m, z_m)}{|J(x_m, y_m, z_m)|} \right|_{\substack{x_m = r_m \sin\theta_m \cos\phi_m \\ y_m = r_m \sin\theta_m \sin\phi_m \\ z_m = r_m \cos\theta_m,}} \tag{5.1}$$

where $J(x_m, y_m, z_m)$ is the Jacobian transformation which is given by

$$J(x_m, y_m, z_m) = \begin{vmatrix} \frac{\partial x_m}{\partial r_m} & \frac{\partial x_m}{\partial \theta_m} & \frac{\partial x_m}{\partial \phi_m} \\ \frac{\partial y_m}{\partial r_m} & \frac{\partial y_m}{\partial \theta_m} & \frac{\partial y_m}{\partial \phi_m} \\ \frac{\partial z_m}{\partial r_m} & \frac{\partial z_m}{\partial \theta_m} & \frac{\partial z_m}{\partial \phi_m}, \end{vmatrix}^{-1} = \frac{1}{r_m^2 \sin\theta_m}. \tag{5.2}$$

Therefore, the AOA joint pdf is given by

$$f(r_m, \theta_m, \phi_m) = r_m^2 \sin\theta_m f(x_m, y_m, z_m). \tag{5.3}$$

The TOA variable can be included in order to determine the AOA and TOA joint pdfs, $f(\tau, \theta_m, \phi_m)$, of the multipath signals as seen from the MS by making use of the Jacobian transformation again. This gives

$$f(\tau, \theta_m, \phi_m) = \left. \frac{r_m^2 \sin\theta_m f(x_m, y_m, z_m)}{|J(r_m, \theta_m, \phi_m)|} \right|_{r_m = \frac{(c^2\tau^2 - D^2)}{2(c\tau + D\sin\theta_m\cos\phi_m)}}, \tag{5.4}$$

where the Jacobian transformation, $J(r_m, \theta_m, \phi_m)$, is given by

$$J(r_m, \theta_m, \phi_m) = \left|\frac{\partial r_m}{\partial \tau}\right|^{-1} = \frac{2(c\tau + D\sin\theta_m\cos\phi_m)^2}{c(c^2\tau^2 + 2c\tau D\sin\theta_m\cos\phi_m + D^2)}. \tag{5.5}$$

Substituting (5.5) into (5.3) and simplifying results in an AOA and TOA joint pdf for a given scatterers density function, $f(x_m, y_m, z_m)$, as given by

$$\begin{aligned} & f(\tau, \theta_m, \phi_m) = \\ & \frac{c\left(c^2\tau^2 - D^2\right)^2 \left(c^2\tau^2 + 2\,c\tau\,D\sin\ \theta_m\cos\phi_m + D^2\right)\sin\theta_m}{8\left(c\tau + D\sin\theta_m\cos\phi_m\right)^4} \times \\ & \qquad\qquad\qquad f(x_m, y_m, z_m), \end{aligned} \tag{5.6}$$

5.4 Model's Verifications

The derived joint pdf is applicable to any distribution of scatterers around the MS. For example, as shown in Figure 4.1, the scatterers are assumed to be distributed uniformly within the spheroid's volume, where the spheroid's volume is limited by τ_{max}. In this case, the scatterers density function, $f(x_m, y_m, z_m)$, is given by $1/V_{\tau_{max}}$. Therefore, the scatterers density function can then be obtained as

$$f(x_m, y_m, z_m) = \frac{6}{\pi c\tau_{max}(c^2{\tau_{max}}^2 - D^2)}. \tag{5.7}$$

Substituting (5.7) into (5.6), results in the joint pdf of the AOA and TOA of the multipath signals as seen from the MS

$$f(\tau, \theta_m, \phi_m) = \frac{3\left(c^2\tau^2 - D^2\right)^2 \left(c^2\tau^2 + 2\, c\tau\, D \sin\ \theta_m \cos\phi_m + D^2\right) \sin\theta_m}{4\pi\tau_{max}(c^2{\tau_{max}}^2 - D^2)\left(c\tau + D\sin\theta_m\cos\phi_m\right)^4}, \tag{5.8}$$

which is equivalent to $f(\theta_m, \phi_m|\tau) \times f(\tau)$ that have been derived in Chapter 4 and given by (4.20) and (4.26), respectively.

5.5 Three Dimensional Gaussian Scatterers Distribution

In the 3D case, the Gaussian expression for a three of random variables (x_m, y_m, z_m) is given by [68]

$$f(x_m, y_m, z_m) = \frac{1}{(2\pi)^{3/2}\sqrt{\sigma_x\sigma_y\sigma_z}} \exp\left(-\frac{1}{2}\left[\frac{(x_m-\mu_x)^2}{\sigma_x^2} + \frac{(y_m-\mu_y)^2}{\sigma_y^2} + \frac{(z_m-\mu_z)^2}{\sigma_z^2}\right]\right), \tag{5.9}$$

where the correlations between these random variables are assumed to be zero. To simplify the formulations, it is also assumed that the expected values are equal to zero, i.e. $\mu_x = \mu_y = \mu_z = 0$, and the variance in the x-axis and the y-axis are assumed to be equal, i.e. $\sigma_x^2 = \sigma_y^2 = \sigma_{xy}^2$. Substituting the aforementioned assumptions into (5.9) and simplifying, results in a simple scatterers distribution density, $f(x_m, y_m, z_m)$, which is given by

$$f(x_m, y_m, z_m) = \frac{1}{(2\pi)^{3/2}\sigma_{xy}\sqrt{\sigma_z}} \exp\left(-\frac{1}{2}\left[\frac{(x_m^2+y_m^2)}{\sigma_{xy}^2} + \frac{z_m^2}{\sigma_z^2}\right]\right), \tag{5.10}$$

where σ_{xy} and σ_z are the standard deviations of the scatterers' density in the horizontal plane, i.e. azimuth, and the vertical plane, i.e. elevation, respectively. These quantities can be used to control the density of the scatterers within the spheroid's volume. Substituting (5.10) into (5.6) and simplifying, results in the following joint pdf of the AOA and TOA for a 3D Gaussian scatterers distribution as given by

$$
\begin{aligned}
f(\tau, \theta_m, \phi_m) = & \\
& \frac{c\,(c^2\tau^2 - D^2)^2\,(c^2\tau^2 + 2\,c\tau\,D\sin\ \theta_m\cos\phi_m + D^2)\sin\theta_m}{8\,(2\pi)^{3/2}\sigma_{xy}\sqrt{\sigma_z}\ (c\tau + D\sin\theta_m\cos\phi_m)^4} \times \\
& \exp\left(-\frac{r_m^2}{2}\left[\frac{\sin^2\theta_m}{\sigma_{xy}^2} + \frac{\cos^2\theta_m}{\sigma_z^2}\right]\right). \qquad (5.11)
\end{aligned}
$$

The model's geometry is symmetrical as seen from both the MS and the BS. However, the scatterers' distributions around the MS and the BS locations are different. Therefore, the joint pdf of the AOA and TOA as seen from the BS/MS locations have different behaviors. The pdfs of the AOA and TOA as seen from the BS, where the scatterers density function at the MS is $f(x_m, y_m, z_m)$, can be obtained by making use of the Jacobian transformation. In this case, the scatterers density model in the Cartesian coordinate system with respect to the BS is given as, $f(x_b, y_b, z_b) = f(x_b - D, y_b, z_b)$, where D is the separation distance of the BS/MS. Similarly, the joint pdf of the AOA and TOA as seen from the BS is given by

$$
\begin{aligned}
f(\tau, \theta_b, \phi_b) = & \\
& \frac{c\,(c^2\tau^2 - D^2)^2\,(c^2\tau^2 - 2\,c\tau\,D\sin\theta_b\cos\phi_b + D^2)\sin\theta_b}{8\,(c\tau - D\sin\theta_b\cos\phi_b)^4} \times \\
& f(x_m, y_m, z_m), \qquad (5.12)
\end{aligned}
$$

where $x_m = r_b \sin\theta_b \cos\phi_b - D$, $y_m = r_b \sin\theta_b \sin\phi_b$ and $z_m = r_b \cos\theta_b$. Substituting these transformation relationships into (5.10) and substituting the results into (5.12) and simplifying, yields

$$
\begin{aligned}
f(\tau,\theta_b,\phi_b) = &\\
&\frac{c\,(c^2\tau^2 - D^2)^2\,(c^2\tau^2 - 2\,c\tau\,D\sin\theta_b\cos\phi_b + D^2)\sin\theta_b}{8\,(2\pi)^{3/2}\sigma_{xy}\sqrt{\sigma_z}\;(c\tau - D\sin\theta_b\cos\phi_b)^4}\times\\
&\exp\left(-\frac{1}{2}\left[\frac{(r_b^2\sin^2\theta_b - 2Dr_b\sin\theta_b\cos\phi_b + D^2)}{\sigma_{xy}^2} + \frac{r_b^2\cos^2\theta_b}{\sigma_z^2}\right]\right), \qquad (5.13)
\end{aligned}
$$

where $r_b = (c^2\tau_m^2 - D^2)/2(c\tau_{max} - D\sin\theta_b\cos\phi_b)$.

5.6 Numerical Results and Model's Validations

To illustrate the behavior of the derived AOA and TOA pdfs based on the proposed 3D Gaussian model, several numerical results are provided. The AOA and TOA marginal pdfs have been plotted at various values of the standard deviations of the scatterers' density in the azimuth and elevation angles. Figure 5.2a shows the graph of the pdf of the AOA in the azimuth angle for different values of σ_{xy}, where $\sigma_z = 1.0$. The graph of the pdf in the elevation angle is shown in Figure 5.2b, for different values of σ_z, where σ_{xy}=2.0. The graphs illustrate a symmetrical behavior around the relative direction between the BS and the MS. Also, the larger values of the scatterers' standard deviation the larger angular spread in both the azimuth and the elevation angles.

The TOA pdf graph is illustrated in Figure 5.2c for different values of σ_{xy}, where $\sigma_z = 0.2$. Clearly, the graph exponentially decreases with an increase in the TOA. These results

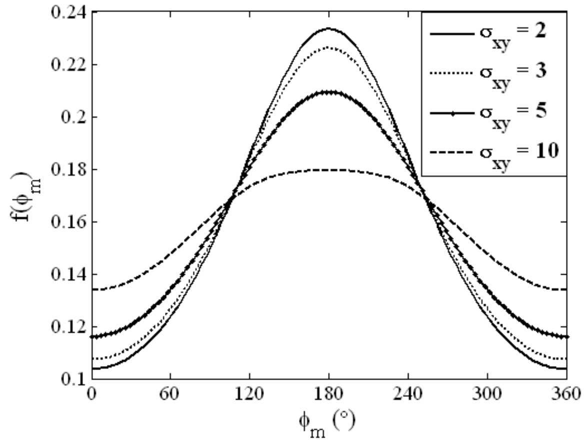

(a) $f(\phi_m)$

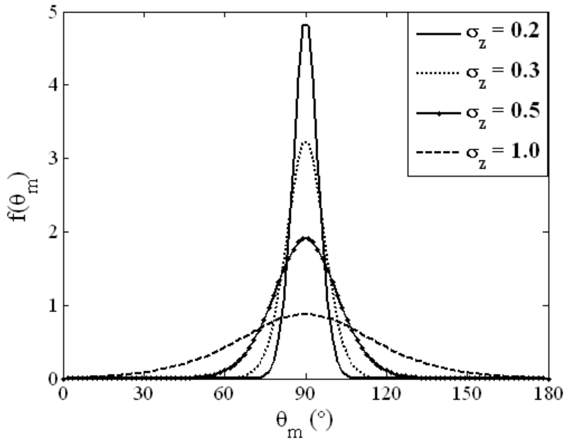

(b) $f(\theta_m)$

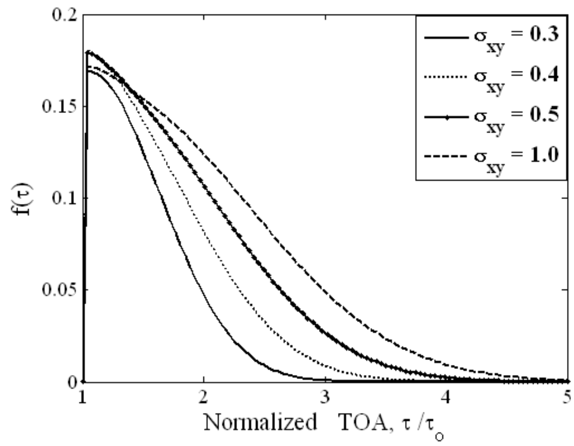

(c) $f(\tau)$

Figure 5.2: The pdfs of the AOA for different values of σ_z and σ_{xy}: a) The pdf of the AOA in the azimuth angle for different values of σ_{xy}, where $\sigma_z = 1.0.$, b) The pdf of the AOA in the elevation angle for different values of σ_z, where σ_{xy}=2.0, and c) The pdf of the TOA for different values of σ_{xy}, for σ_z=0.2.

provide a realistic behavior for the TOA pdf in contrast with the pdf that has been derived based on a uniform distribution of the scatterers. Moreover, the experiments conducted by Pedersen *et al.* in [62] suggest that the TOA pdf in outdoor environments have an exponential distribution.

To validate the 3D Gaussian model, the AOA and TOA pdfs have been compared to the measured channel data available in [45]. Gurrieri *et al.*, in [45], conducted indoor channel measurements at the Communication Research Center (CRC) in Ottawa, Canada. The measurements were made using a network analyzer that generated continuous signals which swept across the 5.10 $\sim$ 5.85 GHz band in 1.875 MHz frequency steps, in order to provide a multipath signals' delay resolution of less than 1.3 ns. The data was collected at two non-LOS indoor locations. The transmitting antenna was a vertically polarized biconical antenna, where the receiving antenna was a square planar array of 8×8 elements. They measured the AOA in both the azimuth and elevation angles, as well as, the TOA of the multipath signals. The results of the measurements show that the multipath signals arrive in clusters in both the AOA and TOA variables. The measured data has been used to generate the AOA and TOA measured pdfs in order to compare them with the theoretical pdfs. The measured AOA and TOA of the multipath signals have been referenced to the first arrival in each location, i.e the first arrival is considered the LOS signal, as in [62]. The AOA of the first arrival signals in the azimuth and the elevation angles are referenced to $\phi_m = 180^o$, and $\theta_m = 90^o$ respectively.

The measured AOA and TOA data has been used to create histograms containing 50 bins. The number of points in each bin was normalized to the total number of points to generate measured pdfs. The marginal pdfs of the AOA and TOA have been integrated in order to convert the continues pdfs to discrete probability mass functions (pmf). Figure 5.3a and Figure 5.3b show the results of comparison in the azimuth and the elevation angles, respectively. Clearly, the distribution of the AOA in the azimuth and the elevation angles are highly peaked along the LOS direction and falls off approximately exponentially away from this direction. The model's parameters were found to be as $\tau_m = 5$, $\sigma_{xy} = 5.0$ and

$\sigma_z = 1.0$ to produce the compared theoretical AOA pmfs. The measured AOA pmf in the elevation angle illustrate almost a uniform distribution within the range of $130^o \sim 150^o$, which is the result of reflections from the ceiling. Figure 5.3c shows the comparison of the theoretical and measured TOA pmfs. The graph illustrate the plots of the pmfs decrease with increasing TOA, τ/τ_o. The model's parameters were found $\tau_m = 5$, $\sigma_{xy} = 0.30$ and $\sigma_z = 0.20$ to produce the compared theoretical pdf. The comparisons of the AOA and TOA pmfs illustrate good agreements between the measured and the derived pmfs. Also, the graphs pmfs of the AOA illustrate non-symmetrical behavior, because the measurements were taken in only two locations. In typical channel measurements, the measured data should be taken in many different locations within different buildings. Furthermore taking the measurements as mentioned may provide better agreement between measured and simulated pmfs of the AOA and TOA. Notice that, the model's parameters, i.e. σ_{xy} and σ_z, were estimated in order to compare with the measured pdfs, based on the measuring relative difference between the two graphs of the pdfs. On other words, the angular spreads have been used in extracting the model's parameters based on the ellipsoid's model which was presented in Chapter 3. However, this technique is unapplicable in extracting the 3D Gaussian model' parameters, because both the azimuth and elevation angular spreads depend on the standard deviations of the scatterers' density in the both azimuth, σ_{xy} angle and elevation angle, σ_z. Similarly, the cosine distance metric has been used to measured the similarity between the theoretical and measured pdfs. Comparisons's results show that the similarity between the pdfs are: 0.9826, 0.9427 and 0.9781 for the: pdf in the azimuth angle, pdf in the elevation angle, and pdf in the TOA, respectively.

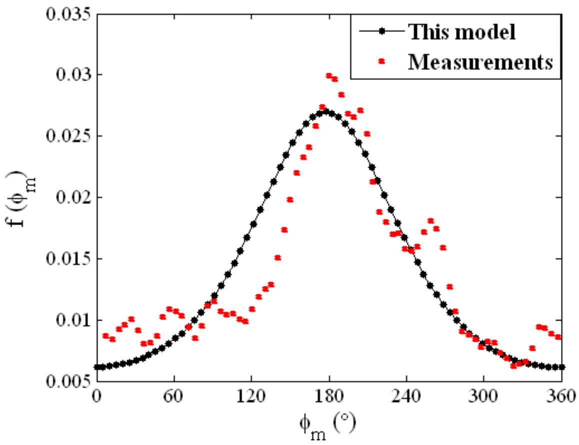

(a) $f(\phi_m)$

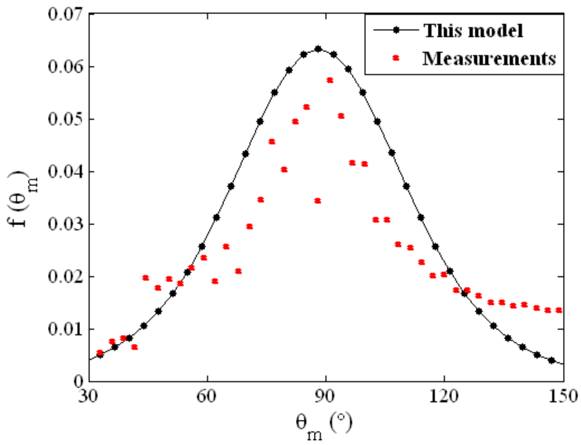

(b) $f(\theta_m)$

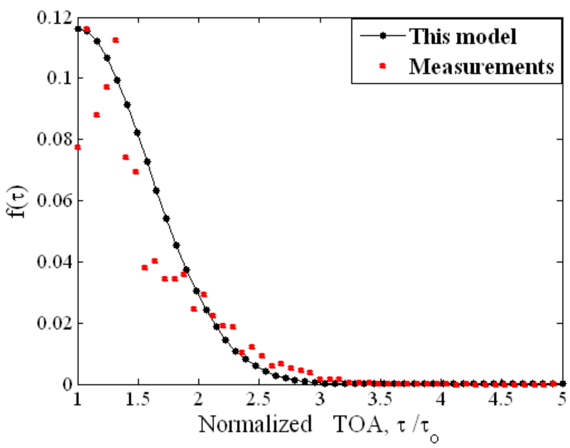

(c) $f(\tau)$

Figure 5.3: Comparison of the AOA and TOA pmfs with measurement data [45]: a) In the azimuth angle, b) In the elevation angle, and c) in the TOA.

Chapter 6

A Three Dimensional Spatial Correlation Function for Multiple Input Multiple Output Wireless Channels

6.1 Introduction

In this chapter, the spatial correlation function of the received multipath fading signals is introduced for MIMO channel modeling applications. This developed 3D spatial correlation function is based on the 3D ellipsoidal model, which is given in Chapter 3. Typically, if the fading between pairs of transmitting and receiving antenna elements are independently and identically distributed, MIMO systems offer a large increase in capacity in contrast to SISO systems. However, in real propagation environments, the fading between different transmitting and receiving antenna elements are not independently, identically distributed, i.e. they are correlated. The correlation between different transmitting and receiving fading signals are the result of many parameters such as: insufficient spacing between antenna elements and non-rich scattering environments.

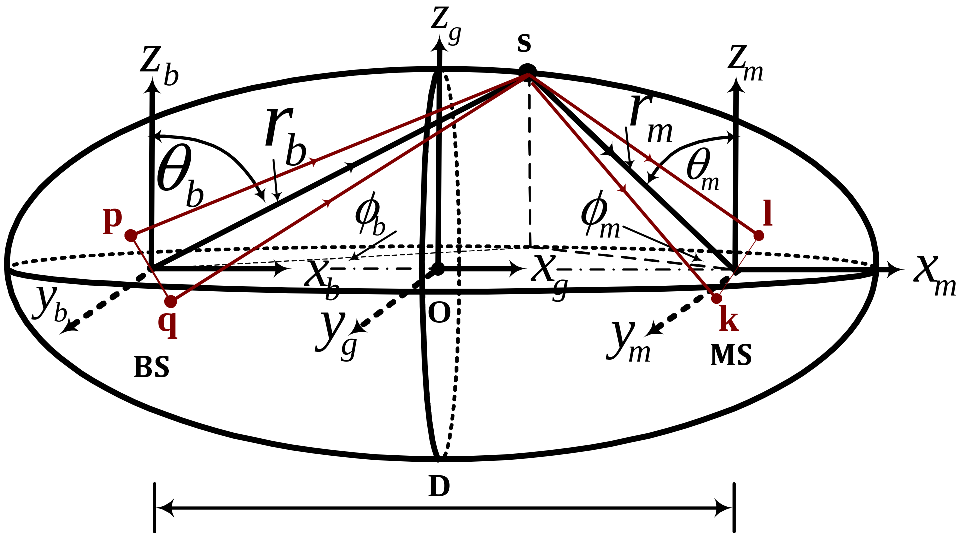

Figure 6.1: 3D MIMO model's geometry.

6.2 Model's Description.

The model's geometry and notations are shown in Figure 6.1. The figure illustrates 2×2 MIMO antenna array for simplification of the derivation, however, the model can be used for any antenna configuration. The transmitting antenna array, i.e. BS, and the receiving antenna array, i.e. MS, antenna elements are centered at the ellipsoid's foci $(\pm D/2, 0, 0)$. The scatterers are assumed to be uniformly distributed within the ellipsoid's volume, but for graphical simplicity, the figure shows only one scatterer denoted by **S**. The transmitting antenna elements are denoted as q and p, while the receiving antenna elements are denoted by k and l. In this case, the distance between the scatterer, **S**, and the transmitting and the receiving antenna elements are denoted by r_q, r_p, r_k, and r_l. As illustrated in Figure 6.2a and Figure 6.2b, the antenna element displacements at the transmitter side are denoted by δ_{qp}, while the corresponding displacements at the receiver side are denoted by δ_{kl}. In the horizontal plane, the receiving and the transmitting antenna arrays are positioned with angles

β_{qp} and β_{kl}, respectively, which are measured from the x-axis. The corresponding angles in the vertical plane are α_{qp} and α_{kl}, respectively, measured from the z-axis. The normalized complex path gain between the q antenna element at the BS, and the k antenna element at the MS can be obtained as

$$h_{kq} = \lim_{S\to\infty} \frac{1}{\sqrt{S}} \sum_{i=1}^{S} g_i \exp\left(j\Psi_i - j\frac{2\pi}{\lambda}(r_{qi} + r_{ik}) \right), \tag{6.1}$$

where S is the number of independent scatterers. g_i and Ψ_i are the amplitude and phase shift introduced by the i^{th} scatterer, respectively. The parameters r_{qi} and r_{ik} are the distances from the scatterer, S_i, toward the transmitting antenna element q, and the receiving antenna element, k, respectively. The total power of the link is given by

$$\Omega_{kq} = \lim_{S\to\infty} \frac{1}{\sqrt{S}} \sum_{i=1}^{S} E\{g_i^2\}. \tag{6.2}$$

The normalized spatial correlational coefficient between the two pairs of channels, k to q and l to q, is given by

$$\rho_{kq,lq} = \frac{E\{h_{kq}h_{lq}^*\}}{\sqrt{\Omega_{kq}\Omega_{lq}}}. \tag{6.3}$$

It has been shown that for a given pdf of the AOA, i.e. $f(\theta_m, \phi_m)$ and the power is equal for all different path links and normalized to be one, i.e. $\Omega_{kq} = \Omega_{lq} = \Omega = 1.0$, then $E\{g_i^2\}/S = f(\theta, \phi)$ [56]. Then, the normalized correlational coefficient can be obtained as

$$\rho_{kq,lq} = \int_0^{\pi} \int_0^{2\pi} \exp\left(-j\frac{2\pi}{\lambda}(r_{qk} - r_{ql}) \right) f(\theta_m, \phi_m) d\phi_m d\theta_m. \tag{6.4}$$

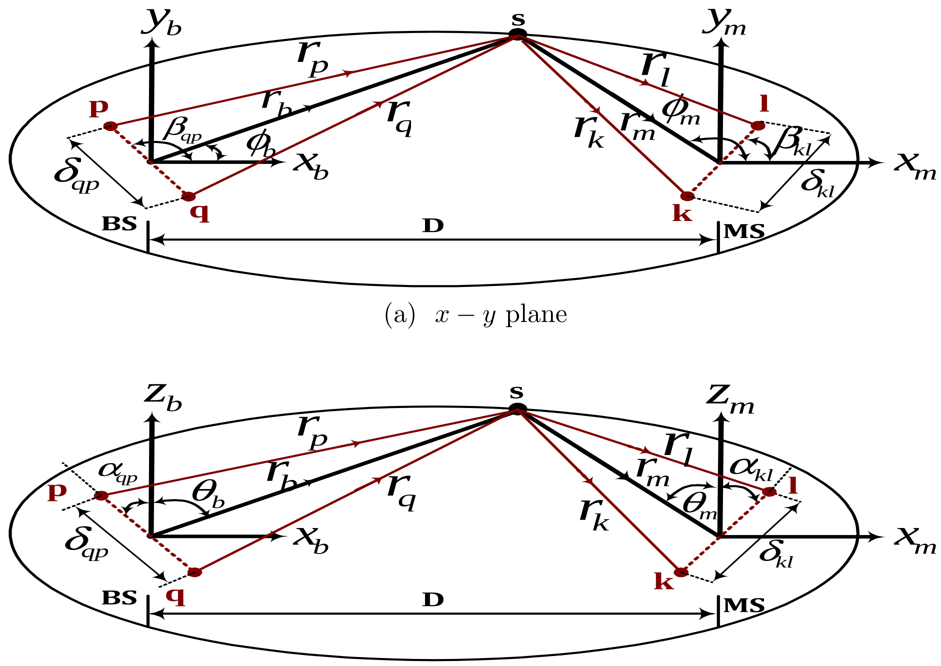

(a) $x - y$ plane

(b) $x - z$ plane

Figure 6.2: Model's geometry in a) $x - y$ plane and b) $x - z$ plane

As shown in Figure 6.1, the locations of receiving antenna elements l and k with respect to the array's center are $(\delta_{kl} \sin \alpha_m \cos \beta_m, \delta_{kl} \sin \alpha_m \sin \beta_m, \delta_{kl} \cos \alpha_m)$ and $(\delta_{kl} \sin(\pi - \alpha_m) \cos(\beta_m + \pi), \delta_{kl} \sin(\pi - \alpha_m) \sin(\beta_m + \pi), \delta_{kl} \cos(\pi - \alpha_m))$ respectively, where the coordinate of the scatterer, **S**, is given by $(r_m \sin \theta_m \cos \phi_m, r_m \sin \theta_m \sin \phi_m, r_m \cos \theta_m)$. Therefore, the difference in distance between the two paths can be approximated as [53–56]

$$r_{qk} - r_{ql} \simeq \delta_{kl} \sin \theta_m \sin \alpha_{kl} \cos(\phi_m - \beta_{kl}) + \cos \theta_m \cos \alpha_{kl}. \tag{6.5}$$

Therefore, the normalized correlational coefficient is given by

$$\rho_{k,l} = \int_0^{\pi} \int_0^{2\pi} \exp\left(-j \frac{2\pi}{\lambda} (\delta_{kl} \sin \theta_m \sin \alpha_{kl} \cos(\phi_m - \beta_{kl}) + \cos \theta_m \cos \alpha_{kl})\right) f(\theta_m, \phi_m) d\phi_m d\theta_m, \tag{6.6}$$

where $f(\theta_m, \phi_m)$ is the AOA pdf that has been derived based on the 3D ellipsoid model. Therefore, the correlation matrix at the receiver side, R_r, can be obtained by making use of equation (6.6). Similarly, due to the symmetry in the model's geometry, the correlation matrix at the transmitter side, R_t, can be obtained by

$$\rho_{p,q} = \int_0^{\pi} \int_0^{2\pi} \exp\left(-j\frac{2\pi}{\lambda}(\delta_{pq}\sin\theta_b \sin\alpha_{pq}\cos(\phi_b - \beta_{pq}) + \cos\theta_b \cos\alpha_{pq})\right) f(\theta_b, \phi_b) d\phi_b d\theta_b. \tag{6.7}$$

6.3 Capacity Multiple Input Multiple Output Systems

The instantaneous channel capacity, in bits per second per hertz, of a stochastic MIMO channel under an average transmitting power constraint, where the transmitter has no channel knowledge, is given by [10, 14].

$$C = \ln\det\left(I_{N_r} + \frac{SNR}{N_t} HH^T\right) \tag{6.8}$$

where I_{N_r} is $N_r \times N_r$ identity matrix, SNR is the average signal-to-noise ratio (SNR), H is the $N_r \times N_t$ complex fading envelopes, $(.)^T$ denotes the transpose conjugate, and $\det(.)$ denotes the matrix determinant. The ergodic capacity of a MIMO channel is defined as the expectation of the instantaneous capacity over time. Hence

$$E[C] = E\left[\ln\det\left(I_{N_r} + \frac{SNR}{N_t} HH^T\right)\right]. \tag{6.9}$$

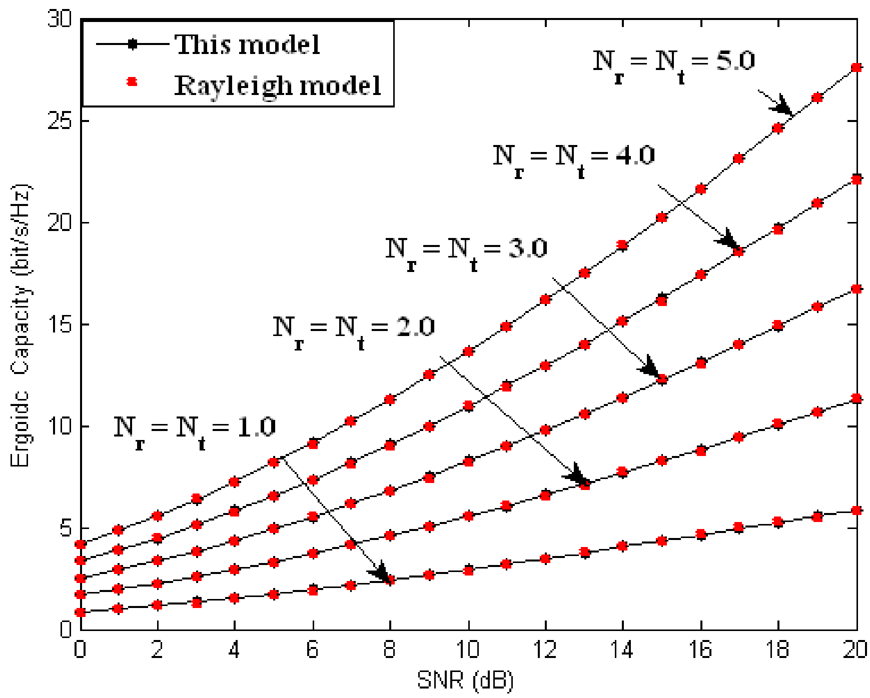

Figure 6.3: Comparison of the ergodic capacities of 5 × 5 MIMO system obtained using the developed 3D model and Rayleigh model

The channel matrix, H, entries are generated by making use of the correlation information of the transmitting and receiving fading signals. This known model is given by [69]

$$H = R_r^{1/2} H_{i.i.d} R_t^{T/2}, \tag{6.10}$$

where $(.)^{1/2}$ denotes the matrix square root operation. R_r is the $N_r \times N_r$ receiving correlation matrix and R_t is the $N_t \times N_t$ transmitting correlation matrix. N_r and N_t are the number of antenna elements at the receiver and the transmitter, respectively. $H_{i.i.d}$ is the $N_r \times N_t$ stochastic matrix with complex Gaussian independently and identically distributed entries.

6.4 Numerical Results and Model's Validations

In this section, several numerical results are provided, to illustrate the effectiveness of the developed 3D spatial correlation model. Figure 6.3 illustrates the ergodic capacities for 5×5 MIMO systems obtained using the developed 3D model and the well known Rayleigh model. The parameters used to obtain the curves Figure 6.3 are $\delta_{kl} = \delta_{pq} = 0.5\lambda$, $\alpha_{kl} = \alpha_{pq} = 90^o$, $\beta_{kl} = \beta_{pq} = 90^o$ and the ellipsoid's eccentricities $e_1 = e_2 \simeq 0.0$, i.e. the ellipsoid's semi-lengths $a \simeq b \simeq c$. The Rayleigh model is based on the assumption that elements of $H_{i.i.d}$ are independent and identical zero mean complex random variables. The graphs show exact agreements between the developed and the Rayleigh models. This results provide the model' verifications and agreed with the fact that for uniform scatterers distribution in 3D space, an antenna elements spacing of $\lambda/2$ is optimal for full decorrelation of the received multipath fading signals [5].

In order to illustrate the different channel physical's parameters, several numerical results are provided. The transmitter's parameters were fixed, while the receiver's parameters were used to investigate the ergodic capacities. The transmitter's parameters were as follows: $\delta_{pq} = 0.5\lambda$, $\alpha_{pq} = 90^o$ and $\beta_{pq} = 90^o$, i.e. the transmitter's elements were along $y-$axis and the ellipsoid' parameters were set as $e_1 = 0.75$ and $e_2 = 0.50$. Figure 6.4, shows the ergodic capacities for 5×5 MIMO systems versus the distance between antenna elements displacements. Clearly, the ergodic capacities decrease with decreasing the displacements of the antenna array. Figure 6.5, shows the performance of the 5×5 MIMO systems versus the orientation angle in the elevation plane, α_{kl}, while the MIMO capacities versus the orientation angle in the azimuth plane, β_{kl} is shown in Figure 6.6. The parameters used to

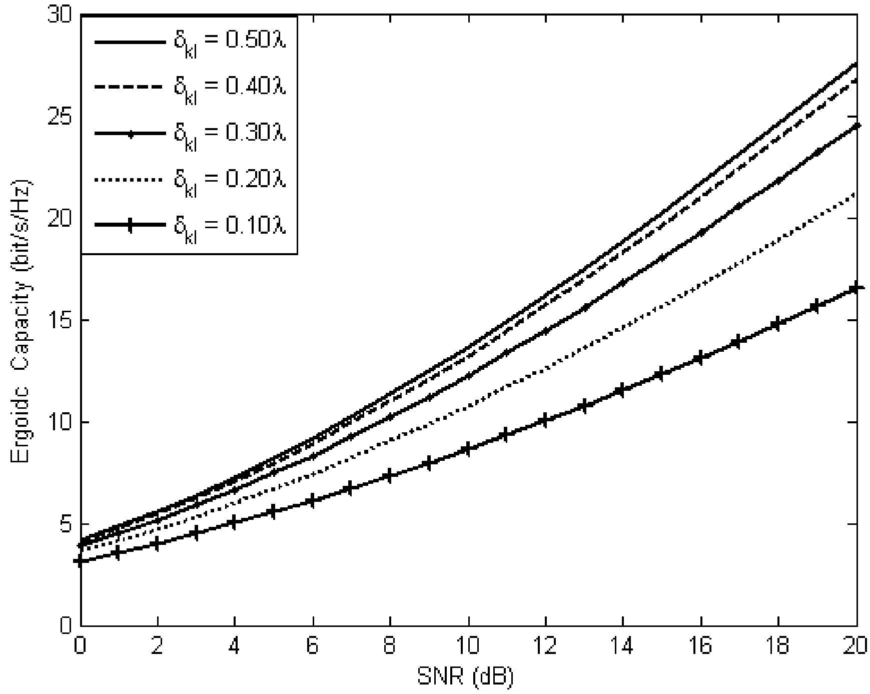

Figure 6.4: Ergodic capacity as a function of spacing between the receiver antenna array elements, δ_{kl}.

obtain the curves Figure 6.5 and Figure 6.6 were $\delta_{kl} = \delta_{pq} = 0.5\lambda$, $e_1 = 0.75$ and $e_2 = 0.50$. Similarly, the effects of the ellipsoid's parameters, which are related to the angular spreads in the azimuth and elevation angles, are shown in Figure 6.7 and Figure 6.8. The figures illustrate that the MIMO capacities are decrease with decreasing the angular spreads in both the azimuth and elevation angles. All the provided graphs illustrate the effectiveness of the proposed 3D spatial correlation model to investigate the performance of the MIMO systems for different channel and antenna arrays conditioners.

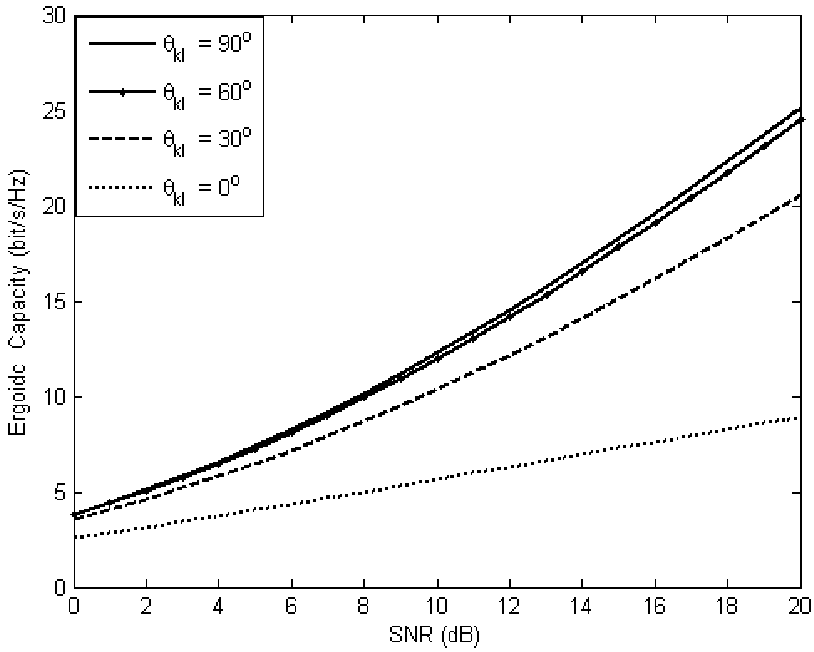

Figure 6.5: Ergodic capacity as a function of antenna array orientation in the elevation angle, α_{kl}.

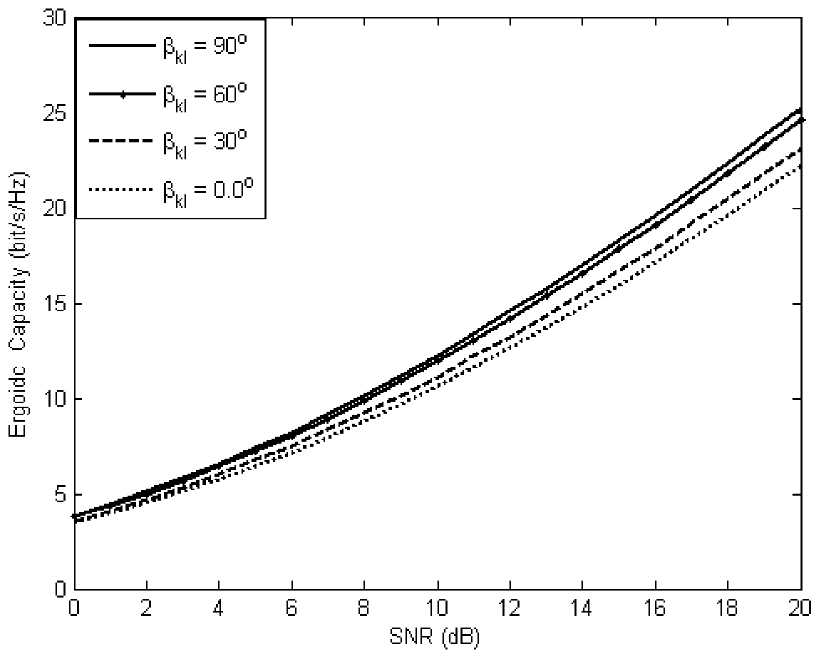

Figure 6.6: Ergodic capacity as a function of antenna array orientation in the azimuth angle, β_{kl}.

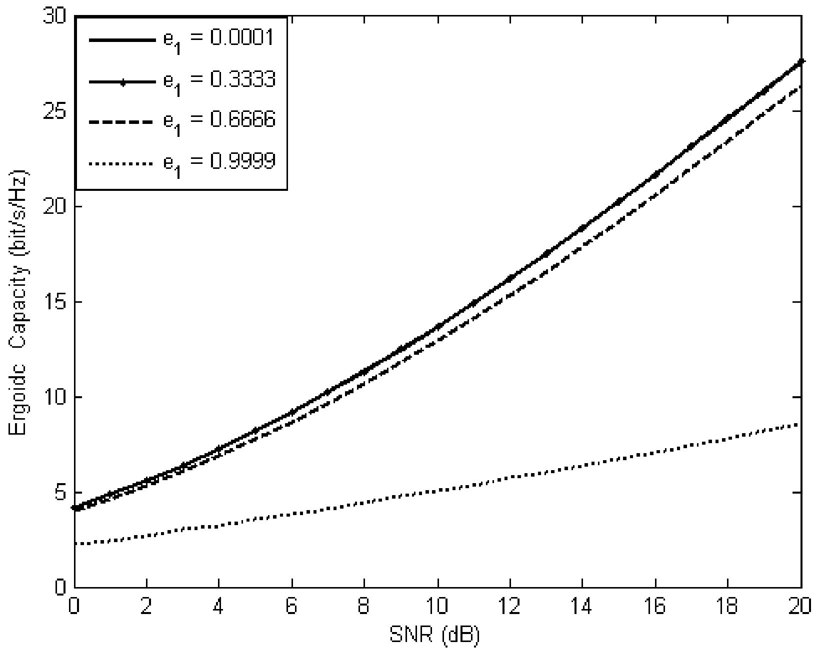

Figure 6.7: Ergodic capacity as a function of the ellipsoid' parameter in the azimuth plane, e_1.

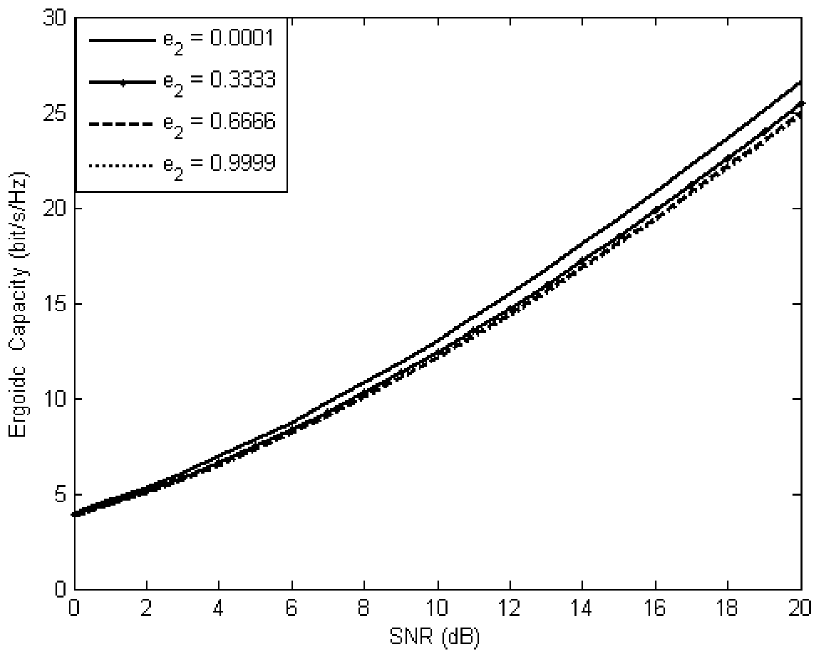

Figure 6.8: Ergodic capacity as a function of the ellipsoid' parameter in the elevation plane, e_2.

Chapter 7

Conclusion and Future Work

7.1 Conclusion

In this thesis, a novel three dimensional (3D) geometrical scattering channel model has been introduced for outdoor and indoor wireless communication environments [46]. Simple formulations have been developed to describe the ellipsoidal geometry as seen from its foci in the Spherical coordinate system. These formulations have been utilized to derive the marginal and joint probability density functions (pdfs) of the angle of arrival (AOA) of multipath fading signals as seen from both the transmitter and receiver, i.e. direction of arrival (DOA) and direction of departure (DOD) of the multipath signals. The new pdfs facilitate independent control of the angular spread in both the azimuth and elevation angles via the model's parameters. These pdfs can be used by wireless systems' providers to design communication hardware more efficiently and optimized the systems' performance in terms of some significant wireless systems metric parameters, such as: capacity, bit-error-rate (BER), number and locations of the base stations (BSs), and co-channel interference cancelation.

In order to verify the developed model an extensive simulations have been done by using a site-specific propagation prediction technique in indoor and outdoor wireless communication environments. The simulations were performed by using the commercially available Wireless InSite software package. The Engineering and Information Technology Complex at the University of Manitoba has been replicated to simulate an indoor radio channel, while the Rosslyn city model was used to simulate an outdoor radio channel. The conclusions that can be drawn from the simulations are as follows: i) the distribution of the AOA in both the azimuth and elevation angle peaked along the relative direction between the transmitter and the receiver. In other words, the most received multipath signals were around the relative direction from the transmitter to the receiver and the symmetries in both the azimuth and elevation planes were obtained, ii) the angular spreads in both the azimuth and elevation angle were found to be dependent on the distance between the transmitter and the receiver. For example, the azimuth angular spread increased with an increase in the distance between the transmitter and the receiver. This result agrees with the assumption that for outdoor macrocellular environments the distribution in the azimuth angle is uniform. On the other hand, the angular distribution in the elevation angle was found to decrease with an increase in the distance. Similarly, this result agrees with the assumption that for outdoor macrocellular environments the transmitted signals propagate on the horizontal plane, i.e. the elevation angular spread is equal to 0.

The channel simulated data have been used to verify the developed new 3D geometrical model. The verification has been achieved by comparing the behavior of the derived and simulated pdfs of the AOA. Comparison results of the AOA pdfs in both the azimuth angle and elevation angle for both the indoor and outdoor scenarios illustrated good agreement between the theoretical and the simulated data [46]. Accordingly, the 3D model can be used to predict statistical characteristics of radio channel in similar wireless communication environments, where the typical values of the radio channel's physical parameters can be found in literature or they can be determined based on the requirements of wireless system designers. Moreover, the model can be used in further study and analysis for the scenarios that have been used to collect the simulated data. This can be achieved by utilizing the verified AOA pdfs to generate the multipath signals for various radio channel physical parameters, such as: angular spread and antenna radiation patterns. To the best of the author's knowledge, the introduced model is the first verified 3D geometrical scattering channel model in literature.

In addition, the 3D ellipsoidal model has been extended in order to take into account the TOA of the received multipath signals. Accordingly, the 3D spheroidal model has been developed with a uniform distribution of scatterers. Several expressions for the AOA and TOA pdfs of the multipath signals have been derived in compact forms [47–49]. The 3D spheroidal model has been verified with a comparison of the AOA pdf in the azimuth angle with the similar 2D models, as well as, with available measured data. The results of the comparisons have illustrated good agreement. To the best of the author's knowledge, the 3D spheroidal model is the first geometrical scattering channel model which incorporates both the AOA in the azimuth and elevation angle, as well as, the TOA of the received multipath signals, i.e. the three random variables of multipath signals. For non-uniform distribution of the scatterers, the 3D spheroidal model has been extended for a general distribution of scatterers around the MS and/or BS. A Gaussian distribution of scatterers has been considered as a case study of a general distribution of scatterers [50]. The joint pdfs of the AOA and TOA i.e. trivariate pdfs, have been provided in compact forms. Also, The

3D Gaussian model has been validated by comparing the derived AOA and TOA pdfs with 3D channel measurements' data. The results of the comparison showed adequate agreement between the theoretical and measured pdfs for all the AOA and TOA parameters. To the best of the author's knowledge, this is the first attempt to illustrate and model the measured AOA pdf in elevation angle, where many pdf of the AOA have been suggested, such as: uniform, sinusoidal, and Gaussian, but without validation.

One advantage of geometrical channel models is ability to have an analytical form of the AOA distributions, for the systems are based on utilizing the space domain. Therefore, the derived pdfs of the AOA based on the ellipsoidal model have been used to derive the spatial correlation function of the received multipath fading signals as seen from both the transmitter and the receiver sides, in order to investigate the performance of MIMO wireless communication systems [51]. This function has been derived in terms of some of the channel's physical parameters, such as: displacement and orientation of the antenna arrays and the delay spread in the azimuth and the elevation angles. Several simulation results have been provided to illustrate the effectiveness of the developed correlation function.

7.2 Future Work

Future work that can build upon the results of this thesis may include the incorporation of the effects of the employed antenna radiation patterns. The developed 2D and/or 3D models are based on the assumption that the antenna radiation patterns are omnidirectional and/or isotropic. However, in real channel environments, the characteristics of the employed radiation patterns have an influence on the received multipath signals. Therefore, extending the pdfs of the AOA and TOA to take into account the radiation pattern effects of the employed antennas is required. Also, investigation of other scatterers' distributions, in this thesis, uniform and Gaussian scatterers' distributions have been investigated. However, other scatterers' density models can be used, such as: cluster distributions or distributions which include the effects of the ground.

Furthermore, the developed 3D channel model can be extended to include other channel and antenna parameters' that have an affect of the received multipath signals. Generally, in geometrical scattering channel models, the power of the received multipath signals is only effected by the distance between the transmitter, scatterer and the receiver, where the scatterers are assumed to be reflecting elements with equal scattering coefficients. Therefore, one can consider including the effects of some important parameters, such as: reflection and diffraction as well as polarization. Also, the inclusion of the employed antenna radiation pattern, as well as, the mutual coupling with the derived spatial correlation function can be consider an extension work. This will provide better prediction for the performance of MIMO wireless systems in order to provide guidelines for efficient designs of MIMO antenna array for different wireless communication environments.

Appendix A

Derivation of the Ellipsoid's Radial Distance as seen From the Focal Point

In the following, the derivation of (3.7) is illustrated. As shown in Fig. 3.1, the intersections of the scatterers volume with the xy and xz planes form two ellipses in which their dimensions on the corresponding axis are assumed to be related as follows

$$\begin{aligned} b &= a\sqrt{1-e_1^2}, && \text{(A.1)} \\ c &= a\sqrt{1-e_2^2}, && \text{(A.2)} \\ f &= e_1 a. && \text{(A.3)} \end{aligned}$$

where e_1, and e_2, are the eccentricity of the ellipses in the xy and xz planes, respectively. Substituting (A.1)-(A.3) into the following formula

$$\frac{(f + r_m \sin\theta_m \cos\phi_m)^2}{a^2} + \frac{r_m^2 \sin^2\theta_m \sin^2\phi_m}{b^2} + \frac{r_m^2 \cos^2\theta_m}{c^2} = 1.0 \tag{A.4}$$

Rearranging terms and simplifying gives

$$r_m^2(\sin^2\theta_m(1-e_1^2)+\cos^2\theta_m(1-e_2^2))-(r_m^2e_1^2(1-e_2^2)\sin^2\theta_m\cos^2\phi_m$$
$$-2r_me_1a\sin\theta_m\cos\phi_m(1-e_1^2)(1-e_2^2)+a^2(1-e_1^2)^2(1-e_2^2))=0 \tag{A.5}$$

Completing the square in the last three terms of the left side and solving for r_m, yields

$$r_m\sqrt{\sin^2\theta_m(1-e_1^2)+\cos^2\theta_m(1-e_2^2)}=$$
$$\pm(r_me_1\sqrt{(1-e_2^2)}\sin\theta_m\cos\phi_m-a(1-e_1^2)\sqrt{(1-e_2^2)} \tag{A.6}$$

Substituting $e_1^2=1-b^2/a^2$, $e_2^2=1-c^2/a^2$ and $e_1=D/2a$ into (A.6) and simplifying; results in the radial distance as seen from the focal point that given by

$$r_m=\frac{2b^2c}{\left(2a\sqrt{b^2\sin^2\theta_m+c^2\cos^2\theta_m}+c\,D\sin\theta_m\cos\phi_m\right)}. \tag{A.7}$$

references

[1] R. Janaswamy, *Radiowave Propagation and Smart Antennas for Wireless Communications*, 1st ed. Kluwer Academic Publishers, 2001.

[2] T. S. Rappaport, *Wireless Communications: Principles and Practice*, 2nd ed. Prentice-Hall, Inc., 2002.

[3] J. C. Liberti and T. S. Rappaport, *Smart Antennas for Wireless Communcations: IS-95 and Third Generation CDMA Applications.* Prentice-Hall, 1999.

[4] M. K. Simon and M.-S. Alouini, *Digital Communication Over Fading Channels.* New York: Wiley, 2000.

[5] A. Paulraj, R. Nabar, and D. Gore, *Introduction to Space-Time Wireless Communications.* Cambridge Univ. Press, 2003.

[6] N. Seshadri and J. Winters, "Two signaling schemes for improving the error performance of Frequency Division Duplex (FDD) transmission systems using transmitter antenna diversity," *Int. J. Wireless Information Networks*, vol. 1, pp. 49–60, Jan. 1994.

[7] R. Heath and A. Paularj, "Transmit diversity using decision directed antenna hopping," in *Comm. Theory Mini conference*, Vancouver, Canada, June 1999, pp. 141–145.

[8] S. Alamouti, "A simple transmit diversity technique for wireless communications," *IEEE J. Sel. Areas Commun.*, vol. 16, no. 8, pp. 1451–1458, Oct. 1998.

[9] A. Paulraj and T. Kailath, "Increasing capacity in wireless broadcast systems using distributed transmission/directional reception," US Patent 5 345 599, 1994.

[10] I. Telatar, "Capacity of multi-antenna gaussian channels," AT & T Bell Laboratories, Tech. Rep., 1995.

[11] R. Roy and B. Ottersten, "Spatial division multipleaccess wireless communication systems," US Patent 5 515 378, 1996.

[12] G. Foschini, "Layered space-time architecture for wireless communication in a fading environment when using multiple antennas," AT& T Bell Laboratories, Tech. Rep., 1996.

[13] V. Tarokh, N. Seshadri, and R. Calderbank, "Space-time codes for high data rate wireless communication: performance criterion and code construction," *IEEE Trans. Inf. Theory*, vol. 44, no. 2, pp. 744–765, Mar. 1998.

[14] G. J. Foschini and M. J. Gans, "On limits of wireless communications in a fading environment when using multiple antennas," *Wireless Personal Commun.*, vol. 6, no. 6, pp. 311–335, Mar. 1998.

[15] I. Telatar, "Capacity of multi-antenna gaussian channels," *European Trans. Telecommun.*, vol. 10, no. 6, pp. 585–595, Nov.-Dec. 1999.

[16] J. C. Liberti and T. S. Rappaport, "A geometrically based model for line of sight multipath radio channels," in *IEEE Vehicular Technology Conf.*, Apr. 1996, pp. 844–848.

[17] P. Petrus, J. H. Reed, and T. S. Rappaport, "Geometrically based statistical channel model for macrocellular mobile environments," in *IEEE Global Telecommunications Conference*, vol. 2, 1996, pp. 1197–1201.

[18] ——, "Effects of directional antennas at the base station on the Doppler spectrum," *IEEE Commun. Lett.*, vol. 1, no. 2, pp. 40–42, 1997.

[19] J. Fuhl, A. F. Molisch, and E. Bonek, "Unified channel model for mobile radio systems with smart antennas," *IEE Proc. -Radar, Sonar Navig*, vol. 145, no. 1, pp. 32–41, Feb. 1998.

[20] O. Norklit and J. Andersen, "Diffuse channel model and experimental results for array antennas in mobile environments," *IEEE Trans. Antennas Propag.*, vol. 46, no. 6, pp. 834–843, June 1998.

[21] R. J. Piechocki, G. V. Tsoulos, and J. P. McGeehan, "Simple general formula for pdf of angle of arrival in large cell operational environments," *Electron. Lett.*, vol. 34, no. 18, pp. 1784–1785, Sep. 1998.

[22] R. B. Ertel and J. H. Reed, "Angle and time of arrival statistics for circular and elliptical scattering models," *IEEE J. Sel. Areas Commun*, vol. 17, pp. 1829–1840, Nov 1999.

[23] P. Petrus, J. Reed, and T. Rappaport, "Geometrical-based statistical macrocell channel model for mobile environments," *IEEE Trans. Commun.*, vol. 50, no. 3, pp. 495–502, Mar. 2002.

[24] R. Janaswamy, "Angle and time of arrival statistics for the Gaussian scatter density model," *IEEE Trans. Wireless Commun.*, vol. 1, pp. 488–497, Jul. 2002.

[25] ——, "Angle of arrival statistics for a 3D spheroid model," *IEEE Trans. Veh. Technol.*, vol. 51, no. 5, pp. 1242–1247, Sep. 2002.

[26] A. F. Molisch, A. Kuchar, J. Laurila, K. Hugl, and R. Schmalenberger, "Geometry-based directional model for mobile radio channels principles and implementation," *European Trans. Telecomm.*, vol. 14, pp. 351–359, 2003.

[27] A. Y. Olenko, K. T. Wong, and E. H.-O. Ng, "Analytically derived TOA-DOA statistics of uplink/downlink wireless multipaths arisen from scatterers on an hollow-disc around the mobile," *IEEE Antennas Wireless Propag. Lett.*, vol. 2, no. 22, pp. 345–348, 2003.

[28] Y. Chen and V. K. Dubey, "Accuracy of geometric channel modeling methods," *IEEE Trans. Veh. Technol.*, vol. 53, no. 1, pp. 82–93, Jan. 2004.

[29] A. Olenko, K. Wong, and M. Abdulla, "Analytically derived TOA-DOA distributions of uplink/downlink wireless-cellular multipaths arisen from scatterers with an inverted-parabolic spatial distribution around the mobile," *IEEE Signal Process. Lett.*, vol. 12, no. 7, pp. 516–519, Jul. 2005.

[30] A. Y. Olenko, K. T. Wong, S. A. Qasmi, and J. Ahmadi-Shokouh, "Analytically derived uplink/downlink TOA and 2D DOA distributions with scatterers in a 3D hemispheroid surrounding the mobile," *EEE Trans. Antennas Propagat.*, vol. 54, no. 9, pp. 2446–2454, Sep. 2006.

[31] T. Imai and T. Taga, "Statistical scattering model in urban propagation environment," *IEEE Trans. Veh. Technol.*, vol. 55, no. 4, pp. 1081–1093, Jul. 2006.

[32] M. R. Arias and B. Manderson, "Clustering approach for geometrically based channel model in urban environments," *IEEE Antennas Wireless Propag. Lett.*, vol. 5, no. 1, pp. 290–293, 2006.

[33] L. Jiang and S. Y. Tan, "Geometrically based statistical channel models for outdoor and indoor propagation environments," *IEEE Trans. Veh. Technol.*, vol. 56, no. 6, pp. 3587–3593, Nov. 2007.

[34] K. N. Le, "A new formula for the angle-of-arrival probability density function in mobile environment," *Signal Process*, vol. 87, no. 6, pp. 1314–1325, June 2007.

[35] K. B. Baltzis and J. N. Sahalos, "A simple 3D geometric channel model for macrocell mobile communication," *Wireless Pers. Commun.*, vol. 51, no. 2, pp. 329–347, Oct. 2008.

[36] N. M. Khan, M. T. Simsim, and P. B. Rapajic, "A generalized model for the spatial characteristics of the cellular mobile channel," *IEEE Trans. Veh. Technol.*, vol. 57, no. 1, pp. 22–37, Jan. 2008.

[37] S. S. Mahmoud, F. S. Al-Qahtani, Z. M. Hussain, and A. Gopalakrishnan, "Spatial and temporal statistics for the geometrical-based hyperbolic macrocell channel model," *Digital Signal Process.*, vol. 18, no. 2, pp. 151–167, Mar. 2008.

[38] I. Jaafar, H. Boujemaa, and M. Siala, "Angle and time of arrival statistics for hollow-disc and elliptical scattering models," in *in Proc. 2nd Int. Conf. on Signals, Circuits and Systems*, Nov. 2008, pp. 1–4.

[39] K. N. Le, "On angle-of-arrival and time-of-arrival statistics of geometric scattering channels," *IEEE Trans. Veh. Technol.*, vol. 58, no. 8, pp. 4257–4264, Oct. 2009.

[40] S. J. Nawaz, B. H. Qureshi, and N. M. Khan, "A generalized 3D scattering model for macrocell environment with directional antenna at BS," *IEEE Trans. Veh. Technol.*, 2010, accepted to be published.

[41] J. Fuhl, J. P. Rossi, and E. Bonek, "High-resolution 3D direction-of-arrival determination for urban mobile radio," *IEEE Trans. Antennas Propagat.*, vol. 45, pp. 672–682, Apr. 1997.

[42] A. Kuchar, J. P. Rossi, and E. Bonek, "Directional macro-cell channel characterization from urban measurements," *IEEE Trans. Antennas Propag.*, vol. 48, no. 2, pp. 137–146, Feb. 2000.

[43] J. Laurila, K. Kalliola, M. Toeltsch, K. Hugl, P. Vainikainen, and E. Bonek, "Wideband 3D characterization of mobile radio channels in urban environment," *IEEE Trans. Antennas Propag.*, vol. 50, no. 2, pp. 233–243, Feb. 2002.

[44] K. Kalliola, H. Laitinen, P. Vainikainen, M. Toeltsch, J. Laurila, and E. Bonek, "3D double-directional radio channel characterization for urban macrocellular applications," *IEEE Trans. Antennas Propag.*, vol. 51, no. 11, pp. 3122–3133, Nov. 2003.

[45] L. E. Gurrieri, T. J. Willink, A. Petosa, and S. Noghanian, "Characterization of the angle, delay and polarization of multipath signals for indoor environments," *IEEE Trans. Antennas Propagat.*, vol. 56, no. 8, pp. 2710–2719, Aug. 2008.

[46] M. Alsehaili, S. Noghanian, D. Buchanan, and A. Sebak, "Angle of arrival statistics of a three dimensional geometrical scattering channel model for indoor and outdoor propagation environments," *IEEE Antennas Wireless Propag. Lett.*, 2010, accepted for publication.

[47] M. Alsehaili, A. Sebak, and S. Noghanian, "A 3D geometrically based ellipsoidal wireless channel model," in *12th International Symposium on Antenna Technology and Applied Electromagnetics (ANTEM2006),*, Jul. 2006, pp. 407–410.

[48] M. Alsehaili, A. R. Sebak, and S. Noghanian, "An improved 3D geometric scattering channel model for wireless communications," in *EMTS 2007 International URSI Commission B - Electromagnetic Theory Symposium*, Ottawa, ON, Canada, July. 26-28 2007.

[49] M. Alsehaili, S. Noghanian, A. Sebak, and D. Buchanan, "Angle and time of arrival statistics of a three dimensional geometrical scattering channel model for indoor and outdoor propagation environments," *Progress In Electromagnetics Research (PIER)*, 2010, accepted for publication.

[50] ——, "Angle and time of arrival statistics for a three dimensional Gaussian scatterers density model," 2010, to be submitted.

[51] M. Alsehaili, A. Sebak, and S. Noghanian, “A 3D geometry-based stochastic channel model (GSCM) for MIMO wireless communication systems,” in *EMTS 2007 - International URSI Commission B - Electromagnetic Theory Symposium*, Ottawa, ON, Canada, July 26-28 2007.

[52] B. Ottersten, “Array processing for wireless communications,” in *Proceedings of workshop on Statistical signal and array processing*, Corfu, Greece, June 1996, pp. 466–473.

[53] S. D. Shiu, G. J. Foschini, M. J. Gans, and J. M. Kahn, “Fading correlation and its effect on the capacity of multielement antenna systems,” *IEEE Trans. Commun.*, vol. 48, no. 3, pp. 502–513, 2000.

[54] A. Abdi and M. Kaveh, “A space-time correlation model for multielement antenna systems in mobile fading channels,” *IEEE J. Sel. Areas Commun.*, vol. 20, pp. 550–560, Apr. 2002.

[55] G. J. Byers and F. Takawira, “Spatially and temporally correlated MIMO channels: modeling and capacity analysis,” *IEEE Trans. Veh. Technol.*, vol. 53, no. 3, pp. 634–643, 2004.

[56] C. Po-Ying and L. Hsueh-Jyh, “Modeling and applications of spacetime correlation for MIMO fading signals,” *IEEE Trans. Veh. Technol.*, vol. 56, no. 4, pp. 1580–1590, 2007.

[57] G. J. Gong, J. F. Hayes, and M. R. Soleymani, “The effect of antenna physics on fading correlation and the capacity of multielement antenna systems,” *IEEE Trans. Veh. Technol.*, vol. 56, no. 4, pp. 1591–1599, 2007.

[58] A. G. Zajic and G. L. Stueber, “Three-dimensional modeling, simulation, and capacity analysis of spacetime correlated mobile-to-mobile channels,” *IEEE Trans. Veh. Technol.*, vol. 57, no. 4, pp. 2042–2054, Jul 2008.

[59] Remcom, *Wireless InSite: Site-Specific Radio Propagation Prediction Software*, 2nd ed., Remcom Inc., 2004.

[60] J.-K. Lee and J. C. Hou, “Modeling steady-state and transient behaviors of user mobility: formulation, analysis, and application,” in *MobiHoc*, 2006, pp. 85–96.

[61] G. Salton and C. Buckley, “Term weighting approaches in automatic text retrieval.” Department of Computer Science, Cornell University, Tech. Rep., Nov. 1987.

[62] K. I. Pedersen, “A stochastic model of the temporal and azimuthal dispersion seen at the base station in outdoor propagation environments,” *IEEE Trans. Veh. Technol.*, vol. 49, pp. 437–447, Mar. 2000.

[63] Q. H. Spencer, B. D. Jeffs, M. A. Jensen, and A. L. Swindlehurst, “Modeling the statistical time and angle of arrival characteristics of an indoor multipath channel,” *IEEE J. Sel. Areas Commun.*, vol. 18, no. 3, pp. 347–360, Mar. 2000.

[64] R. J.-M. Cramer, R. A. Scholtz, and M. Z. Win, "Evaluation of an ultrawideband propagation channel," *IEEE Trans. Antennas Propag.*, vol. 50, no. 5, pp. 561–570, May 2002.

[65] B. Ottersten, "Spatial division multiple access in wireless communications," in *in Proc. Nordic Radio Symp.*, 1995.

[66] C. Ward, M. Smith, A. Jeffries, D. Adams, and J. Hudson, "Characterizing radio propagation channel for smart antenna systems," *Electron. Commun. Eng. J.*, pp. 191–201, Aug. 1996.

[67] M. P. Ltter and P. van Rooyen, "Modeling spatial aspects of cellular CDMA/SDMA systems," *IEEE Commun. Lett.*, vol. 3, pp. 128–131, May 1999.

[68] G. Allan, *An Intermediate Course in Probability*, 1st ed. 223 Springer street, New York, USA: Springer, 1995.

[69] D. Gesbert, H. Bolcskei, D. A. Gore, and A. J. Paulraj, "Outdoor mimo wireless channels: Models and performance prediction," *IEEE Trans. Commun.*, vol. 50, no. 12, pp. 1926–1934, Dec. 2002.